UPPSALA
UNIVERSITET

Digital Comprehensive Summaries of Uppsala Dissertations from the Faculty of Science and Technology 1396

Metal Hydrogen Interaction and Structural Characterization of Amorphous Materials from first principles

ROBERT JOHANSSON

ACTA
UNIVERSITATIS
UPSALIENSIS
UPPSALA
2016

ISSN 1651-6214
ISBN 978-91-554-9635-7
urn:nbn:se:uu:diva-299940

Dissertation presented at Uppsala University to be publicly examined in Å80127, Ångströmlaboratoriet, Lägerhyddsvägen 1, Uppsala, Wednesday, 28 September 2016 at 09:15 for the degree of Doctor of Philosophy. The examination will be conducted in English. Faculty examiner: Professor Peter Mohn (Vienna University of Technology).

Abstract

Johansson, R. 2016. Metal Hydrogen Interaction and Structural Characterization of Amorphous Materials from first principles. *Digital Comprehensive Summaries of Uppsala Dissertations from the Faculty of Science and Technology* 1396. 72 pp. Uppsala: Acta Universitatis Upsaliensis. ISBN 978-91-554-9635-7.

In this thesis, first-principles calculations based on density functional theory have been employed to investigate metal hydrogen interaction in transition, p-block and rare earth metals. Furthermore, the accuracy of the stochastic quenching method was tested in describing the structure of amorphous $Fe_{(1-x)}Zr_x$.

The investigated systems of transition metal hydrides are V-H and $ScZr(CoNi)_2$-H. For V-H, the main focus of the studies is the effect that strain has on the potential energy landscape which governs the metal hydrogen interactions. The investigation has focused on how the properties of hydrogen occupancy in the interstitial sites changes with strain and also how the hydrogen atoms themselves exert strain on the vanadium structure to lower the energy. Results on diffusion, induced strain and zero-point energy are presented which all reveal the considerable difference between tetrahedral and octahedral site occupancy. Diffusion was studied by employing *ab initio* molecular dynamics simulations to obtain diffusion coefficients and to map the movement of the hydrogen atom. A description of hydrogen in vanadium is provided from a fundamental basis that is expected to be applicable to any lattice gas system. For $ScZr(CoNi)_2$-H, the difference of hydrogen occupancy in various interstitial sites and the hydrogen-induced strain was also investigated through calculations of the change in total volume as a function of hydrogen concentration.

The fundamental properties of metal hydrogen bonding were investigated by studying the Zintl phase hydrides that are constituted of the electropositive metal of Nd or Gd and the electronegative metal Ga. Mixing metals of very different electronegativity gives rise to an intricate potential energy landscape in which the incorporation of hydrogen will have a big effect on both the electronic and atomic structure. From the theoretical side of the investigation, structural parameters are presented along with the density of states and Bader charge analysis to describe the hydrogen induced changes to the atomic and electronic structures.

Finally, the accuracy of the stochastic quenching method in describing amorphous $Fe_{(1-x)}Zr_x$ was evaluated by comparing simulated and measured EXAFS spectra. Once the structural agreement had been established the simulated structures were characterized through radial distribution functions and an analysis of the short-range order from Voronoi tessellation. The structural changes with respect to the composition parameter x were also evaluated.

Keywords: hydrogen, vanadium, zintl, laves, strain, diffusion, amorphous, dft, molecular dynamics, md

Robert Johansson, Department of Physics and Astronomy, Materials Theory, Box 516, Uppsala University, SE-751 20 Uppsala, Sweden.

ISSN 1651-6214
ISBN 978-91-554-9635-7
urn:nbn:se:uu:diva-299940 (http://urn.kb.se/resolve?urn=urn:nbn:se:uu:diva-299940)

For my family.

List of papers

This thesis is based on the following papers, which are referred to in the text by their Roman numerals.

I **Effect of uniaxial strain on the site occupancy of hydrogen in vanadium from density-functional calculations**
R. Johansson, R. Ahuja, O. Eriksson, B. Hjörvarsson, and R. H. Scheicher
Scientific Reports 5, 10301 (2015)

II **Effect of tetragonal distortion on the diffusion of hydrogen in vanadium studied with *ab initio* molecular dynamics**
R. Johansson, G.K Pálsson, R. Ahuja, O. Eriksson B. Hjörvarsson, and R. H. Scheicher
Under review in Physical Review B

III **Hydrogen in vanadium: Site occupancy and isotope effects**
X. Xin, R. Johansson, M. Wolff and B. Hjörvarsson
Physical Review B 93, 134107 (2016)

IV **The influence of site occupancy on diffusion of hydrogen in vanadium**
L. Mooij, W. Huang, S.A. Droulias, R. Johansson, O. Hartmann, X. Xin, H. Palonen, R.H. Scheicher, M. Wolff and B. Hjörvarsson
Under review in Physical Review Letters

V **Hydrogen storage properties of the pseudo binary laves phase $(Sc_{1-x}Zr_x)(Co_{1-y}Ni_y)_2$ system**
J. Ångström, R. Johansson, L. H. Rude, C. Gundlach, R. H. Scheicher, R. Ahuja, O. Eriksson, T. R. Jensen and M. Sahlberg
International Journal of Hydrogen Energy, 38, 9772–9778 (2013)

VI **Hydrogenation-Induced Structure and Property Changes in the Rare-Earth Metal Gallide NdGa: Evolution of a $[GaH]^{2-}$ Polyanion Containing Peierls-like Ga−H Chains**
J. Ångström, R. Johansson, T. Sarkar, M.H. Sørby, C. Zlotea, M.S. Andersson, P. Nordblad, R. H. Scheicher, U, Häussermann and M. Sahlberg
Inorganic Chemistry, 55, 345–352 (2016)

VII **Hydrogenation induced structure and property changes in GdGa**
R. Nedumkandathil, V.F. Kranak, R. Johansson, J. Ångström, O. Balmes, M.S. Andersson, P. Nordblad, R. H. Scheicher, M. Sahlberg and U, Häussermann
Journal of Solid State Chemistry, 239, 184–191 (2016)

VIII **Structural characterization of amorphous $Fe_{(1-x)}Zr_x$**
R. Johansson, G. Muscas, S. George, M. Ahlberg, K. Kádas, D. Arvanitis, R. Ahuja, O. Eriksson, R. H. Scheicher and P. Jönsson
In manuscript

Reprints were made with permission from the publishers.

The following papers are co-authored by me but not included in the thesis:

- **Hydrogen Induced Structure and Property Changes in Eu_3Si_4**
R. Nedumkandathil, M. S. Andersson, P. Nordblad, R. Johansson, R. H. Scheicher, U. Häussermann
In manuscript

- **Magnetic Characterization of CoFeZr Thin Films by Combinatorial Sputtering**
A. Frisk, M. Ahlberg, G. Muscas, S. George, R. Johansson, P. Jönsson and G. Andersson
In manuscript

My contribution to the papers

I have performed all first-principles calculations in the listed papers. I have written the Papers I and II as these papers are entirely comprised of data produced by me. The other papers contain both experimental work and first-principles studies. These papers were written in close collaboration with several co-authors where I was responsible for the computational parts.

Contents

1. Introduction

Throughout the history of scientific research, the tools available to the scientists to either make experimental observations, or to predict them theoretically, has evolved steadily during the ages with one era replacing the other. The evolution of the tools can, e.g., be classified by considering what wavelengths in the electromagnetic spectrum we are able to accurately observe. With the advent of techniques to control X-ray radiation, we could observe wavelengths of the order of magnitude corresponding to atomic distances, i.e. angstrom. The various properties of materials that could be observed in the visible part of the electromagnetic spectrum or by mechanical measurements, could now be attributed to the atomic structures and the bonding between atoms. With light ranging from ultraviolet to infrared we can investigate the collective excitation of atoms to describe properties that involve several atoms on the length scale of nano to micrometers. We can predict electronic, optical, mechanical, and thermal properties of model systems and even certain classes of realistic materials purely on theoretical grounds. From simple models we have since the advent of quantum mechanics and solid state theory been able to perform calculations with pen and paper on the dispersion relation of electrons in periodic potentials, e.g., crystalline solids in the limit of free electron gas or tight-binding approximation.

These developments make it today possible to qualitatively understand a new material before performing any measurements, as results from theoretical calculations offer detailed insights into the electronic and structural properties. The limitations of the calculations, that we have always been faced with, is the proper account of many-body interactions. An account of pairwise interaction enables us to present a comprehensive theoretical analysis, however even in this case we are limited by approximations we use in our calculations. There are, however, nowadays, good methods for solving these problems, such as the Density Functional Theory (DFT), which is a first-principles method that was suggested already in 1964 (Ref.1). At that time the computational resources were very limited but it was also the time when a lot of progress was made on integrated circuits that would see computers evolve very quickly. With faster computers and more efficient approximations we have been able to improve the accuracy and the number of atoms in the simulations. Despite the computational power of today, the calculations of properties on the nanoscale, that require several hundreds of atoms, are very costly if we aim for a better accuracy. The primitive lattices are sufficient for calculations of the electronic dispersion relation, whereas proper treatment of vibrational degrees of freedom

(phonons) requires a repetition of the primitive cell in the form of a supercell. There are many reasons why different sized unit cells are needed and a few of them will be presented in this thesis as it is a recurring topic of discussion.

The work presented in this thesis is divided into three different chapters, two of which concern hydrogen in metal and one that concerns amorphous structures. The majority of the presented data on hydrogen in metal treat the long-ranged elastic effect via hydrogen induced strain. From the experimental side, the required time- and length-scales to observe these strain effects can be achieved in for instance Nuclear Magnetic Resonance (NMR) or Neutron Scattering. We investigate the dynamical effects of hydrogen in vanadium employing *ab-initio* Molecular Dynamics (AIMD) where the forces between the atoms are treated quantum mechanically. The diffusion of hydrogen in vanadium is, in relative terms, very fast [2]. The limited time scales of AIMD will, due to high computational cost, only allow us to study physical phenomena on a time scale in the nanoseconds range. This is however enough in this system for us to be able to calculate statistically valid diffusion coefficients at elevated temperatures. We also employ a large supercell to be able to treat the hydrogen atoms as isolated. We will show that, due to significant anisotropy, a large number of atoms is needed to describe the hydrogen-induced strain.

A great advantage of DFT simulations, and theoretical work in general, is the ability to explore what lies beyond the limitations of what is currently experimentally possible. Properties such as temperature, pressure and, for this thesis an important property, strain, can all be easily varied to investigate any part of a phase diagram for a larger number of materials. Theoretical work is also idealized in the sense that we have exact knowledge of the number of atoms in the simulations and their structural parameters. We are however limited to only work with structures constituted of atoms in the thousands, whilst a representation of a macroscopic sample would require a very large number of atoms (cf. 1 g of vanadium contains $\sim 1.2 \cdot 10^{22}$ atoms). A macroscopic sample would also contain defects and/or several structural phases.

Simulating an amorphous material requires a large supercell to replicate long-range disorder. A real space representation of X-ray absorption measurements in the shape of radial distribution function (RDF) for an amorphous material will only show very weak indication of structural order after the first few coordination peaks [3]. We therefore employ sufficiently large supercells that extend to the region of disorder in the RDF. In both the work on hydrogen and the work on amorphous structures we do treat disorder. In both cases, we sample a number of structures until we reach convergence in the average total energy.

The majority of the presented work in this thesis can be considered fundamental research. We investigate the properties of hydrogen in vanadium in Papers I, II, III and IV. We present, what we expect to be, fundamental results applicable to any system of a lattice gas concerning strain fields, diffusion, clamping and lattice-gas phases. In Paper V we investigate the capacity for

hydrogen storage when varying the metal compositions in a quaternary transition metal alloy. In Papers VI and VII we explore the fundamental properties of hydrogen bonding to rare earth gallides, as hydrogen is known to have a strong effect on the electronic structure in both rare earths and p-block elements [4, 5]. In Paper VIII we are studying the structural properties of amorphous iron-zirconium. We compare the real samples investigated by X-ray absorption measurements to structures created with the stochastic quenching method [6–8].

To put the research into a larger perspective, so to answer what the possible applications are, then, for metal-hydrogen, we want to provide a fundamental insight into the metal-hydrogen interactions to drive the search for good hydrogen storage system towards a more knowledge-based approach. With knowledge-based research I refer here to research where there is a good basis of knowledge concerning the fundamental properties before new materials are synthesized and tested. Storing of hydrogen in metal offers great potential regarding both volumetric and gravimetric capacity [9–11]. The challenges are many and there is still a long way to go before the goals are met concerning economic viability to use hydrogen as an energy carrier on the large scale. Much of the research today is oriented towards sampling different materials in search of one that fulfills the set goals. In recent years, though, the progress seems to have stagnated, and I believe that a better understanding of the fundamental properties of hydrides will help guide us towards better materials for applications. Without a doubt, we must at some point become less dependent on fossil fuels because of its effect on the global climate and because it is simply not sustainable in the long term. There is already today a need for energy storage application, as a significant part of the renewable energy is lost because of overproduction. The demand for energy storage applications will, with great certainty, increase in the coming years as we can see a stride towards more self-sustainance regarding energy. As rooftops are being covered by solar panels, the need for either on- or off-site storage of energy will be of great importance.

The motivation behind the work on amorphous iron-zirconium in Paper VIII is to structurally classify the material to relate the systems of various compositions to measured magnetic properties. The exchange interaction, which is responsible for the ferromagnetic effect of iron, is expected to be closely related to the iron-iron distances and the coordination number. We also wanted to validate the stochastic quenching method for amorphous iron-zirconium.

2. Theoretical Background

Density functional theory (DFT) has been widely used in solid-state physics calculations since the 1960s and it has proven to be very successful in many applications, with hydrogen in metals considered in this thesis as being one of them. In this thesis, DFT is the tool used to tackle the many-body problems of hydrogen in metals and amorphous iron-zirconium. The systems that we are modeling do not exhibit strong correlation which can be difficult to deal with using DFT [12]. Furthermore, the considered materials in this thesis are treated as non-magnetic.

2.1 The Many-Body problem

In general, it is very difficult to provide an exact treatment of quantum mechanical systems containing more than two identical particles as we then are dealing with a many-body problem that can not be solved analytically. Developing various approximations to the Schrödinger equation, taking into account periodic boundary conditions and including corresponding interactions between the particles into the Hamiltonian, we can extract information that relates to a macroscopic sample of the material being investigated.

$$\hat{H}\Psi = E\Psi \,. \tag{2.1}$$

The many-body Hamiltonian that properly treats all relevant interactions can be written as

$$\hat{H} = \hat{T}_e + \hat{T}_n + \hat{V}_{nn} + \hat{V}_{ee} + \hat{V}_{ne}, \tag{2.2}$$

where
$\hat{T}_e$ The kinetic energy of the electrons
$\hat{T}_n$ The kinetic energy of the nuclei
$\hat{V}_{ee}$ Coulomb-interaction between the electrons
$\hat{V}_{nn}$ Coulomb-interaction between the nuclei
$\hat{V}_{ne}$ Coulomb-interaction between the electrons and nuclei
Writing out these terms explicitly gives

$$\hat{H} = -\frac{\hbar^2}{2m_e}\sum_{i}^{N_{el}}\nabla^2 - \frac{\hbar^2}{2}\sum_{k}^{N_{nuc}}\frac{\nabla^2}{M_k}$$
$$+\frac{1}{2}\sum_{i\neq j}^{N_{el}}\frac{e^2}{|\mathbf{r}_i-\mathbf{r}_j|} + \frac{1}{2}\sum_{k\neq l}^{N_{nuc}}\frac{Z_k Z_l e^2}{|\mathbf{R}_k-\mathbf{R}_l|} - \sum_{i,k}^{N_{el},N_{nuc}}\frac{Z_k e^2}{|\mathbf{r}_i-\mathbf{R}_k|}. \tag{2.1}$$

In the following sections we present the most common ways of dealing with the many-body problem in first-principles calculations.

2.2 Born-Oppenheimer approximation

The rest mass of protons and neutrons is roughly 1800 times larger than that of an electron. This allows us, in an adiabatic approximation, to consider the motion of the electrons and nuclei to be independent. In basic terms, we say that the wave function is separable and can be factorized into its electronic and nuclear components,

$$\Psi_{tot} = \Psi_{el} \times \Psi_{nuc}. \tag{2.3}$$

The nuclei are thus treated as being stationary and the Coulomb interaction between the electrons and the nuclei is treated as if the electrons were moving in an external potential ($\hat{V}_{ext}$). The Coulomb interaction between stationary nuclei can therefore be left out of the Hamiltonian to be added later to the total energy. With the nuclei considered as being stationary and the Coulomb-interaction between nuclei treated as a contribution to the total energy that can be added later. We can now simplify the Hamiltonian

$$\hat{H} = -\frac{\hbar^2}{2m_e}\sum_{i}^{N_{el}}\nabla^2 + \frac{1}{2}\sum_{i\neq j}^{N_{el}}\frac{e^2}{|\mathbf{r}_i - \mathbf{r}_j|} + \hat{V}_{ext}. \tag{2.4}$$

Any other external field present can be added to the term $\hat{V}_{ext}$.

The many-electron eigenfunction is very difficult to calculate since all electrons interact with each other. Summing over the number of electrons, N, there is a total of $\frac{N}{2}(N-1)$ number of Coulomb-interactions present between the electrons. Also considering that each electron has 3 degrees of freedom, giving the system a total of $3N$ degrees of freedom. One way to vastly simplify the system is to introduce a density functional which is purely determined by the electron density $n(\mathbf{r})$ as an argument that has only 3 degrees of freedom. The density functionals and their use will be discussed in the next section.

2.3 Hohenberg-Kohn theorems

The paradigm of DFT is based on the two theorems by Hohenberg and Kohn [13].

1. The external potential $V_{ext}(\mathbf{r})$ in a system of interacting particles is determined by the ground-state electron density $n_0(\mathbf{r})$.
2. For any external potential, there exists a universal energy functional $F[n]$. The minimum value of the energy functional for a specific external potential $V_{ext}(\mathbf{r})$ is the ground state energy where the density that minimizes the functional is the ground state density $n_0(\mathbf{r})$.

2.4 Kohn-Sham ansatz

To further simplify the problem we employ the Kohn-Sham (KS) ansatz [14]. It states that an "artificial" system of non-interacting particles in an effective potential consisting of an external part (denoted as $\hat{V}_{ext}$) and an exchange-correlation part that originates from the electron-electron interactions, will have the same ground state electron density $n_0(\mathbf{r})$ as a system with interacting particles. In the KS ansatz, the ground state total energy functional is written as

$$E_0[n(\mathbf{r})] = T[n(\mathbf{r})] + \int V_{ext}(\mathbf{r})n(\mathbf{r})\mathrm{d}\mathbf{r} + \frac{1}{2}\iint \frac{n(\mathbf{r})n(\mathbf{r}')}{|\mathbf{r}-\mathbf{r}'|}\mathrm{d}\mathbf{r}\mathrm{d}\mathbf{r}' + E_{xc}[n(\mathbf{r})] + E_{II}, \tag{2.5}$$

where E_{II} denotes the energy contribution from nuclei-nuclei interaction. $T[n(\mathbf{r})]$ is the kinetic energy of the non-interacting particles. Since the particles are treated as non-interacting, the individual orbitals can be solved separately with the single-particle KS equation

$$\left\{-\frac{1}{2}\nabla^2 + V_{eff}(\mathbf{r})\right\}\psi_i(\mathbf{r}) = \varepsilon_i\psi_i(\mathbf{r}), \tag{2.6}$$

where the single-particle orbitals are determined by diagonalization of the KS-Hamiltonian. The effective potential is composed of three parts: the external potential, the Hartree (or Coulomb) energy and the exchange-correlation energy,

$$V_{eff}(\mathbf{r}) = V_{ext}(\mathbf{r}) + V_H(\mathbf{r}) + V_{xc}(\mathbf{r}), \tag{2.7}$$

where the charge density can be written as

$$n(\mathbf{r}) = \sum_{i=1}^{N} |\psi_i(\mathbf{r})|^2. \tag{2.8}$$

The KS equations are then solved iteratively with a self-consistent method until a set value ΔE in the energy difference between two consecutive iterations is reached. First, one makes a guess for the charge density $n(\mathbf{r})$ to be used to calculate the effective potential $V_{eff}(\mathbf{r})$. This potential is then used in the one-particle KS equation to compute the orbitals which are used to calculate a new charge density that can be fed back into the loop as a new guess.

We cannot solve the exchange-correlation potential exactly as it is what separates our non-interacting system from an interacting one and we do not know what it is, hence we must instead find a good approximation. It is crucial to find a good approximation as the success of DFT, to a large extent, depends on it. In the next section we will discuss a few approaches that can be used for this.

2.5 Exchange and correlation functionals

One of the simplest exchange-correlation functionals is a functional that only depends on the charge density at each point in space. These type of functionals are referred to as Local Density Approximations (LDA) and they originate from a homogeneous electron gas model

$$E_{xc}^{LDA}[n] = \int n(\mathbf{r})\varepsilon_{xc}[n(\mathbf{r})]\mathrm{d}\mathbf{r}, \tag{2.9}$$

where $\varepsilon_{xc}[n(\mathbf{r})]$ is the exchange-correlation energy density, which is a function of the density alone. To improve on this functional a gradient can be added so that the exchange-correlation does not merely depend on the density in each point in space but also on the rate at which the charge density varies. This type of functional is called a Generalized Gradient Approximation (GGA). One of the more widely used GGA functionals, which has also been employed in this thesis, is the Perdew, Burke and Ernzerhof (PBE) functional [15, 16].

2.6 Bloch theorem

In a crystal with translational symmetry, a translational operation $\hat{T}$ to find equivalent points in the crystal is defined as

$$\mathbf{T} = u_1\mathbf{a}_1 + u_2\mathbf{a}_2 + u_3\mathbf{a}_3, \tag{2.10}$$

where u_1,u_2,u_3 are integers and $\mathbf{a}_1$,$\mathbf{a}_2$,$\mathbf{a}_3$ are the lattice vectors. In a periodic lattice, the orbitals can be chosen in agreement with the Bloch wave function

$$\Psi_k(\mathbf{r}) = u_k(\mathbf{r})e^{i\mathbf{k}\cdot\mathbf{r}}, \tag{2.11}$$

where $\mathbf{k}$ is a vector in the first Brillouin zone and $u_k(\mathbf{r})$ is a function with the same periodicity as the crystal lattice, i.e. $u_k(\mathbf{r}) = u_k(\mathbf{r}+\mathbf{T})$. The Bloch theorem [17, 18] thus states that, for a translationally invariant potential, the corresponding wave function is periodic. Therefore, we can reduce the size of our periodic system to the size of the unit cell, for which we need to find an applicable form of $u_k(\mathbf{r})$.

2.7 Projector augmented-wave method

The projector augmented-wave method (PAW)[19, 20] is used in electronic structure calculations to reduce the computational cost by transforming the plane wave basis near the atomic core to a smooth wave function. The plane-waves needed to describe the core electrons will oscillate rapidly and it will thus require an infinite number of Fourier components to describe them, thus making it computationally heavy to include an accurate description of them.

The smooth wave functions are called pseudo wave functions and they are used near the core region to describe non-valence electrons. In the PAW method a linear operator $\hat{\tau}$ transforms the fictitious pseudo wave functions to the KS single-particle functions (usually referred to as all-electron wave function)

$$|\Psi\rangle = \hat{\tau}|\tilde{\Psi}\rangle = (\hat{\mathbf{1}} + \sum_a \hat{\tau}^a)|\tilde{\Psi}\rangle, \tag{2.12}$$

where $\hat{\tau}^a$ only acts inside the core region and a is the atom index. While in the core-region, the pseudo wave function is more practical to be used to describe the non-valence electrons, we require it to be identical to the all-electron wave functions outside the core-region. In the core-region (Ω_R), the pseudo waves can be expanded into partial waves

$$|\tilde{\Psi}\rangle = \sum_i |\tilde{\phi}_i\rangle c_i \ \text{ within } \ \Omega_R. \tag{2.13}$$

The corresponding all-electron wave function can then be written as

$$|\Psi\rangle = \hat{\tau}|\tilde{\Psi}\rangle = \sum_i |\phi_i\rangle\, c_i \ \text{ within } \ \Omega_R. \tag{2.14}$$

We require the transformation τ to be linear which means that the coefficients c_i are linear functions of the pseudo wave functions and can be obtained by multiplication with some projector function

$$c_i = \langle \tilde{p}_i | \tilde{\phi}_i \rangle. \tag{2.15}$$

There is exactly one projector function per pseudo partial wave and the projector function must fulfill the condition

$$\sum_i |\tilde{\phi}_i\rangle\langle \tilde{p}_i| = 1 \ \text{ within } \ \Omega_R, \tag{2.16}$$

which implies that

$$\langle \tilde{p}_i | \tilde{\phi}_j \rangle = \delta_{ij}. \tag{2.17}$$

The transformation operator $\hat{\tau}$ can now be written as

$$\hat{\tau} = \hat{\mathbf{1}} + \sum_i (|\phi_i\rangle - |\tilde{\phi}_i\rangle)\langle \tilde{p}_i|. \tag{2.18}$$

Applying the transformation on the Hamiltonian of the KS fictitious system will reduce the computational demand by transforming the plane wave basis in the core-region for a “smooth” function.

2.8 Hellman-Feynman forces

A system of atoms which are not in an equilibrium state will have a non-zero net force acting on them. The force can be calculated from the derivative of

the total energy with respect to the spatial coordinates of the atoms

$$\mathbf{F} = -\frac{\partial E}{\partial \mathbf{R}}. \tag{2.19}$$

The Hellman-Feynman theorem allows us to relate the derivative of the energy to the expectation value of the derivative of the Hamiltonian of the system. In Dirac notation, the Hellman-Feynman theorem is written as

$$\begin{aligned} \mathbf{F} = -\frac{\partial E}{\partial \mathbf{R}} = -\frac{\partial}{\partial \mathbf{R}} \langle \Psi | \hat{H} | \Psi \rangle = \\ - \langle \Psi | \frac{\partial \hat{H}}{\partial \mathbf{R}} | \Psi \rangle - \left\langle \frac{\partial \Psi}{\partial \mathbf{R}} \middle| \hat{H} | \Psi \right\rangle - \langle \Psi | \hat{H} \left| \frac{\partial \Psi}{\partial \mathbf{R}} \right\rangle. \end{aligned} \tag{2.20}$$

At the exact ground state solution, the energy is extremal with respect to all possible variations of the wave function and the two last terms thus cancel out.

From the KS approach the only non-zero terms left after derivation with respect to $\mathbf{R}$ are

$$\mathbf{F} = -\int \frac{\partial V_{ext}(\mathbf{r})}{\partial \mathbf{R}} n(\mathbf{r}) \mathrm{d}\mathbf{r} - \frac{\partial E_{II}}{\partial \mathbf{R}}. \tag{2.21}$$

2.9 Zero-point energy

The zero-point energy is the lowest possible energy of a quantum mechanical system. In the vicinity of a local minimum in the potential energy function, the lowest-order change in energy is proportional to the square of the atomic displacement. The zero-point energy can be easily obtained for a harmonic oscillator which is in the lowest possible energy state allowed by Heisenberg's uncertainty principle.

Through second-order polynomial fit, we can obtain the spring-constant k analogous with the classical spring potential function, i.e.

$$V(x) = \frac{1}{2} k x^2 = \frac{1}{2} m \omega^2 x^2, \tag{2.22}$$

so that

$$\omega = \sqrt{\frac{k}{m}}. \tag{2.23}$$

The lowest energy of a harmonic oscillator is given by

$$E = \frac{(\Delta p)^2}{2m} + \frac{1}{2} m \omega^2 (\Delta x)^2. \tag{2.24}$$

Minimizing this function using the lower limit of the uncertainty principle

$$\Delta x \Delta p = \frac{\hbar}{2}, \tag{2.25}$$

gives the ground state energy of a harmonic oscillator

$$E = \frac{\hbar\omega}{2}. \tag{2.26}$$

Zero-point energy corrections are particularly important for the hydrogen atoms in a metal-hydrogen system as the light hydrogen atoms possess a much larger oscillation frequency than the heavier metal atoms, as can be seen from equation 2.23.

3. Transition metal-hydrogen

Transition metals are elements with partially filled d subshells; all elements in group 3 to 12 are transition metals along with a few of the lanthanides that also exhibit the same properties. There are many classes of metal-hydrogen systems, some of them form compounds with stoichiometric chemical formulas and some do not. In this chapter, we present results on non-stoichiometric interstitial metal-hydrogen systems with variable amounts of hydrogen [21, 22]. Our results contribute to the study of vanadium-hydrogen systems. Vanadium is a good model system for studies on metal-hydrogen interaction because of its very favorable kinetics [2]. The frequency of diffusion events is very high in vanadium-hydrogen (VH), thus, a large quantity of statistical data can be obtained in a short simulation time. This allows us to calculate statistically accurate diffusion coefficients. We believe that our findings for the vanadium-hydrogen system will help us understand the fundamentals of site occupancy and diffusion in all transition metal-hydrogen systems. An important factor that partly governs the diffusion is the hydrogen induced strain fields [23, 24]. In the VH system, we have studied both local and global effects of hydrogen induced strain [25–30]. In Paper V we have investigated the hydrogen storage capacity of the c15 Laves phase $(Sc_{1-x}Zr_x)(Co_{1-y}Ni_y)_2$-$H_z$, where the focus is on the global effect of hydrogen induced strain (i.e. change in volume due to hydrogen uptake).

Interstitial metal-hydrogen systems are defined by the hydrogen atoms being situated in cavities in the lattice, i.e. interstitial sites [21, 22]. It is a bit misleading to refer to interstitial metal-hydrogen systems as compounds because the term "compounds" usually implies that the hydrogen is strongly bound to the metal through covalent bonds. Interstitially bound hydrogen atoms are however held in place largely by metallic bonds, i.e. electrostatic forces between free electrons and nuclei in the material. The metal and hydrogen atoms form solid solutions where the dissociated hydrogen molecules are seen as the solute in a metallic solvent, usually referred to as the α-phase. This disordered α-phase is the most common phase at low hydrogen concentration and/or high temperature [2]. There are several ordered phases for higher hydrogen concentrations at lower temperatures, usually denoted by β or γ [2, 21, 22]. Transitions between different hydrogen phases are often accompanied by a structural change of the hosting metal [23, 26, 31, 32] which in turn can give rise to various changes to other properties which we investigate in Paper I and II.

An important distinction in the work on vanadium is the **uniaxial** and **biaxial** strains. In Paper I we want to mimic the experimental condition of hydrogen uptake in clamped thin films where the hydrogen induced strain is

uniaxial. In Papers II and IV we want to mimic the experimental condition of in-plane clamping [26, 31] which causes a tensile strain in the out of plane direction, hence "biaxial". In the experiments, the vanadium films are grown and held on substrates through strong bonds that do not allow in-plane movement of the vanadium atoms on the substrate. When hydrogen is absorbed, the volume expansion of the vanadium film is only allowed in the out-of-plane direction perpendicular to the substrate. The in-plane dimensions (width) are much larger that the out-of-plane extension (thickness) of the films (centimeters Vs. nanometers) so that any "bulging" on the sides of the films can be neglected. Figure 3.1 is a simple schematic illustration of hydrogen uptake in a substrate-bound vanadium film.

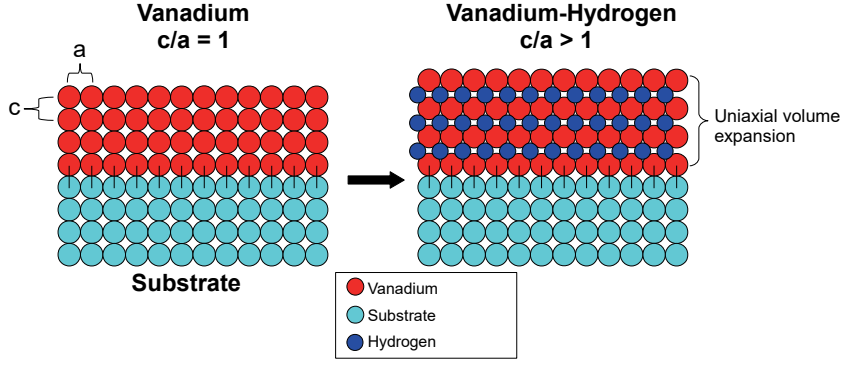

Figure 3.1. Visualization of hydrogen uptake in a substrate-bound vanadium film.

The thin films used in Papers III and IV for the experimental measurements are called superlattices and as the name suggests their design is a bit more sophisticated than a homogeneous thin film. A superlattice is a periodic structure consisting of bilayers of two or more different materials. The ratio of the number of layers of the constituent materials in the bilayer is used to tailor the properties of the superlattice. The material sandwiched between the vanadium layers is usually one with a much lower hydrogen solubility so that only a very small fraction of hydrogen atoms, at any given time, will reside there. Iron has a very low solubility of hydrogen atoms but still offers fast kinetics, i.e. absorbed hydrogen atoms will quickly diffuse through the iron layers. There is, however, a mismatch in lattice constants between vanadium and iron ($d_{Fe} = 2.87$ Å and $d_V = 3.04$ Å), which causes a biaxial tensile strain of the vanadium layers and a biaxial compressive strain of the iron layers in the out of plane direction. Different strain states can be induced by altering the ratio of the vanadium to iron layers. When the bilayers of vanadium are thin, i.e. only a few atomic layers, the finite-size and interface effects will have a big impact on the physical properties of hydrogen absorption [33]. In our DFT simulations, we neglect any such effects as we only study bulk proper-

ties. In Papers III and IV, the layers of vanadium in the superlattices used are 21 monolayers thick, which corresponds to roughly 60 Å. We therefore make the approximation to treat vanadium as bulk in our model calculations since the interface regions are small in relation to the "inner" part of the vanadium layers.

3.1 Computational setup

In Chapter 2 we briefly introduced density functional theory (DFT). The described theory is implemented in several software packages for atomic scale modeling of materials. For our calculations we opted to use the Vienna *Ab initio* Simulation Package (VASP) [34–37]. The used version of VASP in Paper **I** has been modified by the Swedish National Infrastructure for Computing (SNIC) to allow us to perform constrained cell relaxation.

The interactions between the electrons and the nuclei were calculated using the projector-augmented-wave method [19, 38]. The generalized gradient approximation (GGA) in the parametrization of Perdew-Burke-Ernzerhof (GGA-PBE) [15, 16] was employed to approximate the exchange and correlation terms in the DFT [1, 14] method. The GGA-PBE method has proven to be very successful when dealing with transition metal-hydrogen systems in the past [30, 31]. A conjugate gradient algorithm was used to relax the atomic nuclei positions to a local minimum in the total energy landscape.

When performing calculations to determine preferred site occupancies and volume expansion due to hydrogen induced strain, we need to take a few things into consideration when setting up the system. The system needs to be large enough so that at the lowest possible hydrogen concentration, the hydrogen atom can be treated as isolated, i.e. very small H-H interaction due to periodic boundary conditions. The system should be big enough so that at a greater hydrogen concentration (e.g. [H/V]=0.5), the hydrogen can be distributed in a disordered fashion to mimic an α-phase solid solution. We can, on the other hand, expect that a large number of computations will be needed for any study involving hydrogen induced strain effects in an α-phase solid solution, thus, the system can not be exceedingly large because that would require too much computational effort.

For the studies on vanadium in Papers I, II and IV, a 128 atoms body-centered cubic *bcc* supercell has been used, corresponding to a $4 \times 4 \times 4$ repeat of the 2 atoms *bcc* unit cell and 11.9 Å $\times$ 11.9 Å $\times$ 11.9 Å in volume for the unstrained case, i.e. $c/a = 1.00$. To mimic the experimental conditions of clamped thin films on substrates, the supercell is constrained in the x and y-directions during relaxation of the volume. Volume expansion/compression of the supercell is thus only allowed in the z-direction (corresponding to the out-of-plane expansion of the vanadium film when absorbing hydrogen). A 128 atoms body-centered tetragonal (*bct*) supercell contains in total 512 T_z,

256 T_{xy}, 128 O_z and 256 O_{xy} interstitial sites, adding up to a total of 1152 high symmetry sites (see Figure 3.2). For the study on vanadium in Paper III, different small size supercells were used to accommodate various hydrogen concentrations.

For the c15 Laves structure, only the 24 atoms primitive cell was used with its 8 b-, 32 e-, and 96 g-sites (see Figure 3.3). Apart from different unit cells, only the number of k-points used to sample the Brillouin zone differs in the computational setup between the two investigated systems. The Γ point alone was used for the large VH system, while a $9 \times 9 \times 9$ k-point grid was employed for the smaller c15 Laves structure.

3.2 Interstitial sites

As a simple approximation, we can consider a solid metal as being constituted of stacked spherical atoms. When stacking spheres, not all space is filled, for instance, the body-centered cubic structure has a packing efficiency of $\sim$68%. That leaves 32% of the *bcc* unit cell for other atomic species to occupy. All the transition metal atoms are significantly larger than the hydrogen atom, the interstitial space found in the metal lattices can thus hold many hydrogen atoms before overlapping orbitals causes large Born-Mayer repulsion [39]. The largest interstitial site, i.e. the point in the *bcc* primitive cell where the nearest neighboring atom is as far away as possible, is called a tetrahedral site. The second largest type of high symmetry interstitial in the *bcc* cell are the octahedral sites.

If the *bcc* cell is uniaxially strained, thus forming a *bct* structure with $a = b \neq c$, formerly equivalent tetrahedral sites split into different sites, denoted by T_z and T_{xy}, and likewise octahedral sites split into O_z and O_{xy}. The tetrahedral and octahedral sites are illustrated in Figure 3.2. No distinction is made between the x and y-oriented sites since they are equivalent in a *bct* lattice strained along the z-direction. They are identical in the sense that a rotation by 90° around the z-axis will map the x-sites onto the y-sites, and vice versa.

The c15 Laves structure is an AB_2 type of structure that has three unique types of tetrahedral sites which are the preferred sites for hydrogen occupation. The tetrahedral sites are illustrated in Figure 3.3. Can we predict which type of site will be energetically favorable for the hydrogen to occupy based on the geometry of the sites? Adopting a hard sphere model allows us to calculate the maximum sphere radius that can be accommodated in the interstitial space formed by the metal atom spheres arranged in a *bcc* pattern. In units of the metal atom sphere radius, the results are 0.155 for octahedral and 0.291 for tetrahedral sites. For most transition metals, hydrogen uptake is an exothermic reaction, i.e. the hydrogen atoms lowers their energy after being absorbed by forming hydrogen-metal bonds. For the transition metals that absorb hydro-

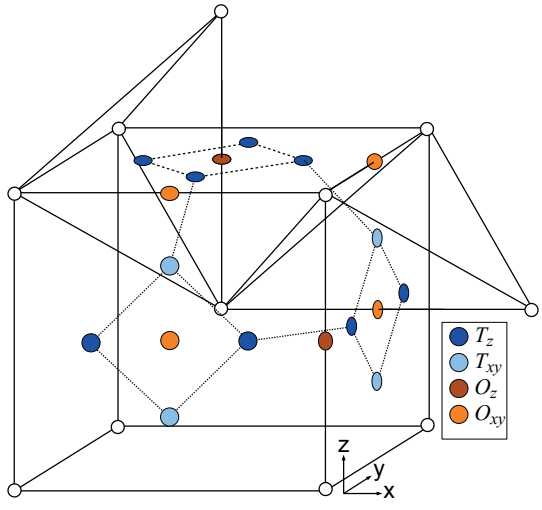

Figure 3.2. (a) Tetrahedral and (b) octahedral sites for the *bcc* cell. Large dark spheres represent vanadium atoms and the small red, blue, light blue, and light red spheres represent (according to their respective labels) different interstitial positions that hydrogen can occupy. The z-axis is aligned along the vertical direction, while the x- and y-axes lie in the horizontal plane.

gen via endothermic reactions, there is typically large Born-Mayer repulsion due to large overlap of the electronic orbitals, i.e. the interstitial sites are too "narrow" [39].

A potential energy function can be expressed as the sum of a repulsive term due to the overlap of electronic orbitals and an attractive term as a result of electrostatic forces from sharing free electrons. Figure 3.4, from Ref.2, is a plot of the energy of an H atom in an environment with a homogenous charge density of magnitude n_0. The minimum represents the most energetically favorable charge density for H occupancy. Most metals, including vanadium, have interstitial sites with a charge density that is higher than the density which yields the lowest energy of H occupancy.

Much of the work conducted on vanadium is aimed at investigating the effect on the energetics of the hydrogen atoms when we alter the shape and size of the interstitial sites by straining the vanadium lattice [23, 32, 40, 41].

3.2.1 Self-trapping

Self-trapping is a term used to describe the effect the hydrogen atom has on the potential energy landscape [30, 42]. We will define the self-trapping energy as the difference in energy before and after relaxation of the metal lattice when a hydrogen atom is residing in an interstitial site. Figure 3.5 is a simple illustra-

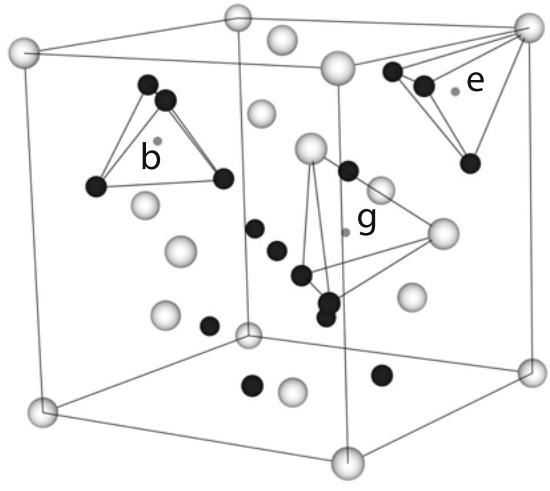

Figure 3.3. c15 Laves structure with three unique interstitial tetrahedral sites denoted by b,e and g. The larger lighter spheres are A-atoms in a AB_2 constellation and the smaller darker spheres are B-atoms.

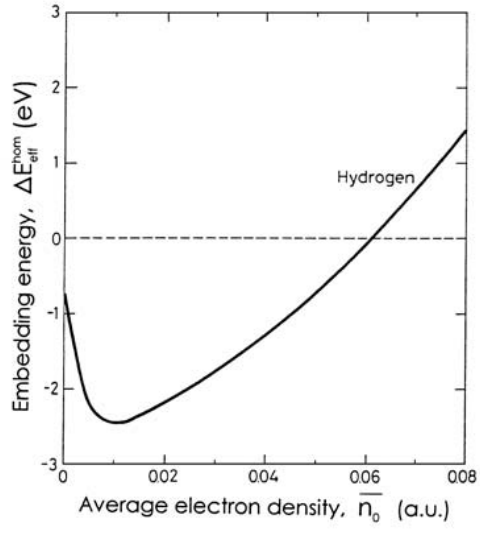

Figure 3.4. Hydrogen embedding energy as a function of surrounding charge density.

tion of self-trapping of a hydrogen atom (red dot) in a periodic potential. The full line indicates a one-dimensional projection of the potential energy landscape experienced by a hydrogen atom in a metal lattice when the hydrogen has not been allowed to exert strain on the metal lattice atoms. The dotted

line indicates the potential landscape experienced by the hydrogen atom after relaxation of the metal lattice atoms.

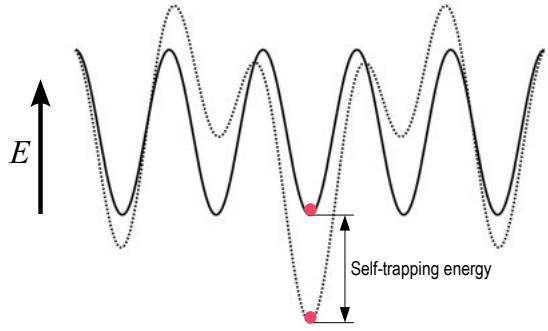

Figure 3.5. Illustration of self-trapping. The full and dashed lines indicate the potential energy landscape experienced by a hydrogen atom in one dimension before and after relaxation of the hosting lattice, respectively. The red dot indicates a hydrogen atom.

3.2.2 Effect of uniaxial tensile strain on preferred site occupancy

When uniaxially straining a lattice, we increase the volume. Figure 3.6 is a simple illustration using a hard sphere model to compare the interstitial volumes of the T_z and O_z sites before and after a uniaxial strain of 20%. The spheres are fixed in the geometrical centers of the T_z and O_z sites, respectively. Initially the T_z site can house the largest sphere, but when uniaxially straining

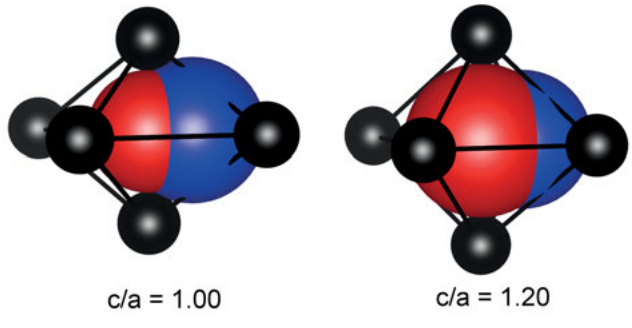

Figure 3.6. Visualization of the hard sphere model to compare interstitial volumes of T_z (blue sphere) and O_z (red sphere) sites when uniaxially straining the lattice.

the lattice, the O_z site eventually becomes the largest. When also including the local strain fields caused by the hydrogen atoms, the predicted shift in site occupancy, based on energetics of hydrogen occupancy in the T_z and O_z sites,

occurs within the investigated range of c/a (i.e. 1.00–1.07). As one might expect, it is found that the critical strain [23, 32, 40, 41] of equality in energetics of hydrogen occupancy and the critical strain of equal interstitial volume, are in fact of similar magnitude.

Figure 3.7, taken from Paper I shows the result of DFT calculations for the energy of a single hydrogen atom in a 128 vanadium atoms supercell occupying either a T_z, T_{xy}, O_z or an O_{xy} site as a function of c/a.

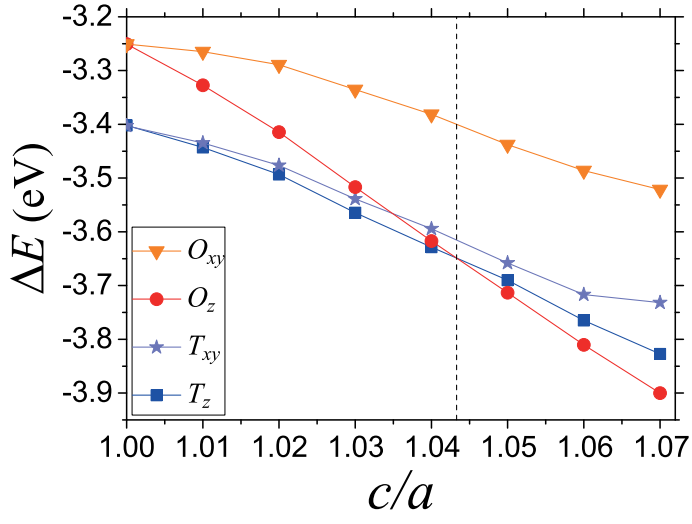

Figure 3.7. Energy difference as a function of an externally applied global uniaxial lattice strain c/a where $\Delta E = E(V+H) - E(V)$. The dashed vertical line at $c/a = 1.043$ marks the critical uniaxial lattice strain for which hydrogen occupancy of T_z and O_z sites become energetically equivalent.

When uniaxial tensile strain is applied, the volume is increased. At $c/a = 1.043$, the O_z sites becomes energetically favorable. When the volume of the interstitial sites is altered, so is the charge density, with an increase in the volume corresponding to a decrease in charge density. For vanadium, in the c/a range of 1.00 to 1.07, the energy of hydrogen occupancy is lowered for all sites. Decreasing the charge density is thus energetically favorable for H occupancy in vanadium (c.f. Figure 3.4). Furthermore, we know from simple geometrical considerations that the increase in volume of the O_z sites from uniaxial strain proceeds at a higher rate than that of the T_z sites (see Figure 3.6) and that the volume of O_{xy} sites remains unchanged since the "top" and "bottom" atoms of the constituent atoms in those octahedra are fixed. Thus, the energy of hydrogen site occupancy in the O_{xy} decreases at a much lower rate with respect to c/a than that of O_z site occupancy (see Figure 3.7).

3.2.3 Zero-point energy and isotope effect

We have investigated the isotope effect of hydrogen and deuterium in vanadium from both experiments and first-principles calculations in Paper III.

The phase diagrams of V_2H and V_2D exhibits different ordering temperatures [22, 43], in which, the different vibrational energy of the hydrogen and deuterium has been identified as a major cause of this [44]. In our calculations we compare the enthalpy of formation between hydrogen and deuterium in both T and O_z sites. In the experiments, the data referring to T site occupancy (α phase) is that of bulk vanadium, while the data referring to O_z sites occupancy (β phase), is that of Fe/V superlattices.

The zero-point energy (ZPE) is the result of a particle being trapped in a potential well with the condition that the particle behaves like a quantum harmonic oscillator in the ground state, i.e. the energy of the particle is $E = \hbar\omega/2$ at T=0K. The hydrogen atoms in a vanadium lattice will experience different potential landscapes in the various interstitial sites and it is reasonable to assume that, with strain, the potential landscapes in the various sites changes differently [2]. In our studies on hydrogen in vanadium in Papers I–IV, we often refer to the hydrogen as being confined to sites and that there is a level of confinement associated with a particular site. With the level of confinement we mean the "narowness" of the potential energy well. The hydrogen atom has 3 degrees of freedom and consequently there are 3 vibrational modes. The force constant k and the corresponding normal coordinates of the vibration can be found by diagonalization of the Hessian matrix (square matrix of second-order partial derivatives). In the work on hydrogen and deuterium in vanadium we neglect the vibrational energy of the vanadium atoms as the vanadium atom is approximately 51 times heavier than hydrogen (and 25.5 times heavier than deuterium). We also consider an adiabatic approximation when calculating the vibrational energy of the hydrogen atoms, i.e. the potential energy landscape is approximated as being frozen during the vibration of the hydrogen atoms.

Different size supercells were used to accommodate the hydrogen atoms for the three investigated concentrations of [H/V]=0.25, 0.50 and 1.00. For the concentration of 0.25 we used a supercell of the size $(1\times1\times4)$ bcc unit cells. Because of the large polarization of the local strain field induced by the hydrogen atoms in the O_z sites we have opted to use a supercell of ample size that allows for placement of the hydrogen atom such that the overlap of the strain fields is significantly reduced and consequently also the energy. In simpler terms we can say that hydrogen atoms in O_z sites does not want the nearest neighbouring hydrogen atoms to occupy a site in the z-direction. The strain field is isotropic in the case of T site occupancy but despite that we employ a $(1\times1\times4)$ supercell to reduce the numerical errors when comparing the energetics of hydrogen in T and O_z sites. The enthalpy of formation is

calculated with the formula:

$$\Delta h = \frac{E[V+H(D)] - (E[V] + \frac{1}{2}E[H(D)_2])}{N_{H(D)}}\,, \tag{3.1}$$

in which, the first term is the energy of the vanadium lattice with the hydrogen (or deuterium) self-trapped in it while the two last terms are the energy of the separate constituents, i.e. the vanadium lattice and the hydrogen/deuterium gas molecule. The total energy of the hydrogen/deuterium gas is calculated by placing the hydrogen/deuterium atoms in an $8\times8\times8$ Å box and relaxing the interatomic distance and calculating the vibrational frequency to get the ZPE correction to the total energy.

The calculations for T site occupancy were performed by using supercells that were allowed to expand or contract without any restrictions during volume relaxation. This is to mimic the effects of hydrogen in bulk vanadium.

For the calculations on O_z occupancy we used supercells, that were constricted to only expand or contract in the z-direction so to mimic the uniaxially constricted volume expansion/contraction of thin films.

In our calculations when comparing the enthalpy of formation for hydrides and deuterides, the difference in energy between the isotopes stems solely from the ZPE. There are no dynamical effects included in the relaxation of the hydrogen/deuterium in the vanadium lattice. The vibrational frequency of hydrogen is a factor $\sqrt{2}$ higher than that of deuterium (see Eq. 2.23) which causes slightly larger induced strain from hydrogen occupancy. The effect is not reproduced in our static calculations.

Table 3.3 shows the calculated enthalpy of formations for the two isotopes and the difference between them. We can see that the isotope effect is greater for the T site occupancy and that the isotope effect essentially does not change with concentration for the O_z site occupancy. The increase in concentration also means an increase in volume and for the case of T site occupancy, with no constraints on the lattice, the volume expansion is uniform. For O_z site occupancy we see the trend that the isotope effect decreases with concentration. Thus, constraining the volume expansion of the vanadium lattice has a profound effect on the potential energy landscape.

The results are in agreement with earlier experimental findings of weaker isotope effect in O_z site occupancy as compared to T site occupancy [22]. It is clear that the ZPE is a contributing factor.

3.2.4 The combinatorics problem

Dealing with a supercell consisting of 128 vanadium atoms for a disordered metal-hydrogen phase means having a very large number of possible hydrogen distributions for a certain concentration. This is because we have 1152 high symmetry sites in our supercell where hydrogen can reside. Ideally we would

Table 3.1. *Formation enthalpies for H and D in T and O_z sites obtained from first-principles calculations. Lattice parameters were fixed at a = b = 2.98 the calculations on the O_z-site occupancy. Volume expansion/contraction was only allowed in the z direction. For T occupancy the unit cells were allowed to expand/contract in all directions.*

Occupancy	c[H(D)/V]	0.25	0.50	1.00
	Δh_H(meV/H)	-251	-260	-292
T	Δh_D(meV/D)	-286	-296	-326
	Δh_H-Δh_D[meV/H(D)]	35	36	34
	Δh_H(meV/H)	-171	-293	-296
O_z	Δh_D(meV/D)	-201	-317	-305
	Δh_H-Δh_D[meV/H(D)]	30	24	9

like to find the ground state configurations for each concentration [H/V], i.e. the hydrogen distribution that yields the lowest total energy of the system. We do however have a finite temperature in the real vanadium-hydrogen system which means that we can not neglect the contribution to the enthalpy from changes in entropy. More order means a decrease in entropy and thus an increase in enthalpy. An increase in entropy can weigh more strongly than a decrease in total energy.

We have adopted a method of randomly distributing hydrogen into our metal supercells and calculating the average total energy and volume. In this manner, we will converge to a certain average energy and volume if we repeat this procedure many times as long as we include a large enough number of random distributions. As an approximation, we do not consider partial occupancies of different types of interstitial sites in neither vanadium nor the Laves system. Also, we do not make any assumptions regarding the preferred distribution of hydrogen in the disordered phase.

Figure 3.8 shows the variation in total energy and equilibrium volume for 50 random distributions of 16 hydrogen atoms in a 128 vanadium atoms supercell for T_z occupancy (c.f. Figure 3.2). As can be seen from the red line, which indicates the average, convergence is reached quite fast. The standard deviation, indicated by the vertical bars, also converges fast. After 50 random hydrogen distributions, the standard deviation is 4.6 meV per atom and 0.00039 in c/a.

3.3 Hydrogen-induced strain

In most metals, the interstitially absorbed hydrogen atoms will initially be more influenced by the repulsive part of the forces than the attractive ones, i.e.

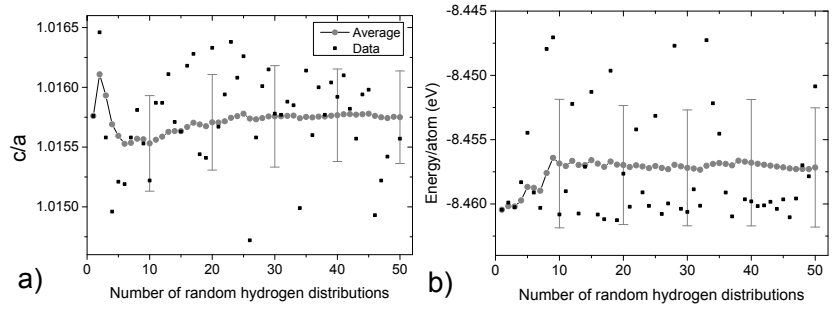

Figure 3.8. Convergence of average c/a (a) and energy (b) for random distributions of 16 hydrogen atoms at T_z sites in a 128 vanadium atoms supercell.

large overlap of the electronic orbitals causing repulsion. The hydrogen will thus repel the metal atoms so to make its interstitial site larger, and thereby reduce the repulsive force. This is however not always the case as there are metals where absorbed hydrogen will attract and thereby retract metal atoms and thus making the interstitial sites smaller. For instance, in amorphous materials where there is a very large range of interstitial sites with different volumes, the hydrogen atoms can explore them to find sites that are very favorable for occupation so that the first few atomic percent of hydrogen being absorbed in the metal essentially keeps the total volume fixed. A difference in volume of the interstitial sites will also mean a difference in charge density. The charge density dependent repulsive and attractive interaction of the hydrogen and metal atoms electrons can be minimized [2, 45, 46]. The most energetically favorable place for hydrogen occupation in transition metals is thus linked to the charge density in the various sites.

Each absorbed hydrogen atom causes a small local strain field in the metal lattice [25–30]. When the hydrogen concentration is increased, the sum of these small local strains combines to give rise to an increase in the volume of the metal lattice. The arrows in Figure 3.9 indicates the displacement of the constituent atoms of the tetrahedral and octahedral sites, respectively, in the *bcc* lattice of vanadium when occupied by hydrogen.

The difference in electronegativity between hydrogen and the host metal atoms can be an indicator of how large these strains will be in various metals. The hydrogen atoms possess larger electronegativity than the metals investigated in this thesis, which causes the hydrogen atom to localize some of the neighboring free electrons [47–49]. The effective charge of the hydrogen atoms is thus negative. This results in the metallic bindings of the surrounding metal atoms to diminish, which in turn allows the hydrogen to repel them more.

The volume increase from hydrogen absorption is nearly linear with increasing concentration for disordered phases [50]. The increase in volume

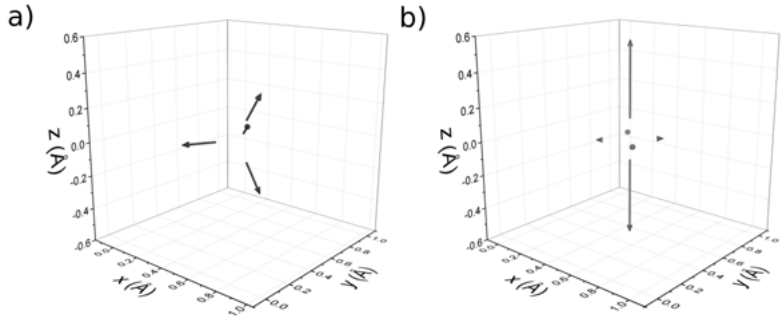

Figure 3.9. The strain on surrounding vanadium atoms by hydrogen occupying a (a) T_z site or (b) O_z site. The arrows represent the displacement vectors, i.e., how much the V atoms are "pushed" away by the H atom. For better visibility, the length of the arrows has been scaled by a factor of 30.

for hydrogen absorption in vanadium is 1.61 Å^3 per added H atom in the low concentration α-phase region. Each vanadium atom occupies 14 Å^3, meaning that to reach a concentration of [H/V]=1 in the α-phase, there would be an 11.4% increase in total volume. The corresponding number for $Sc_{(1-x)}Zr_x(Co_{(1-y)}Ni_y)_2$ is 2.72± 0.14 Å^3 per added H atom for occupancy in the e-sites (see Figure 3.3) for $(x,y) = (0.25, 0.50), (0.50, 0.50)$ and $(0.75, 0.50)$. The e-sites were found to be energetically favorable at low hydrogen concentrations and approximated to be favorable also at higher concentrations ([H/V]=0 to 1.00). The Sc to Zr ratio has a negligible effect on the hydrogen induced volume (see Figure 3.10).

3.3.1 Simulations on volume expansion

Using random distributions of hydrogen in the supercell of vanadium and the unit cell of the c15 Laves phase $(Sc_{1-x}Zr_x)(Co_{1-y}Ni_y)_2$-$H_z$, the following results were obtained when calculating the response of hydrogen being implanted in the metal lattices. In the investigated ranges of hydrogen concentration, H/M from 0 to 1.0 for $(Sc_{1-x}Zr_x)(Co_{1-y}Ni_y)_2$-$H_z$ and 0 to 0.5 for the vanadium-hydrogen system, volume expansion is approximately linear, as shown in Figure 3.10, taken from Paper V. The two datasets in Figure 3.11 show the different responses of the system when hydrogen occupies either T_z sites or O_z sites (c.f. Figure 3.2). The increase in volume due to hydrogen uptake stems from the small strains that each hydrogen atom causes in the metal. As can be seen in Figure 3.9, taken from Paper I, the strain on the constituent atoms in the O_z site is very different from that of the T_z site. The strain field is strongly anisotropic for O_z site occupancy, while it is nearly isotropic for T_z occupancy. Since we have a large strain component in the z-direction for O_z site occupancy and because we only allow volume increase in the z-direction

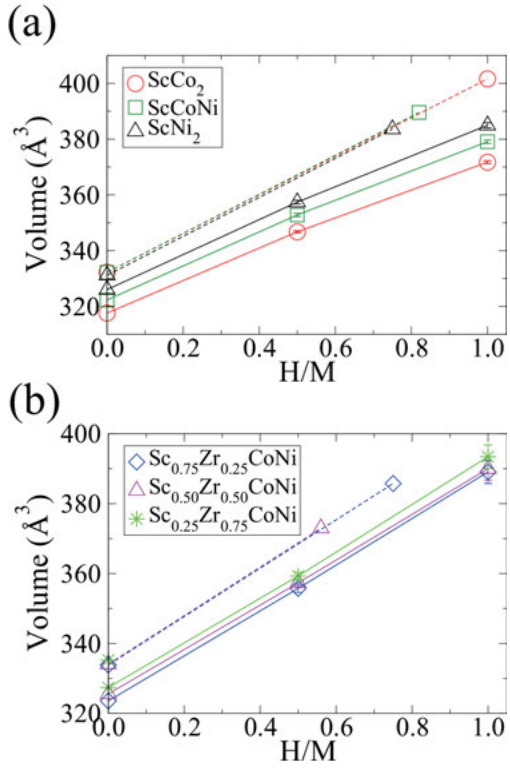

Figure 3.10. Total volume of the C15 Laves phase unit cell as a function of the hydrogen to metal ratio [H/M]. Experimental data is shown as symbols connected by dashed lines while theoretical data is presented by the same set of symbols connected through full lines. The error bars are given by $\pm$ half the standard deviation. In the top panel (a) the amount of Sc is held constant while the ratio of Co to Ni is varied. In the bottom panel (b) the ratio of Co and Ni is held constant while the ratio of Sc to Zr is varied.

to mimic the experimental conditions, we find a much higher rate of increase in volume when occupying O_z sites, as compared to T_z sites.

3.3.2 Change in site occupancy and hysteresis

From Figure 3.7, we know that T_z sites are energetically favorable at low strain for a hydrogen concentration of [H/V]=1/128. If we externally strain the supercell uniaxially by altering c/a, the potential landscape in the various interstitial sites will change according to the slopes of the curves in Figure 3.7. The vertical dashed line at $c/a = 1.043$ indicates where the curves of T_z and O_z cross. This means that the O_z sites are energetically favorable for $c/a > 1.043$.

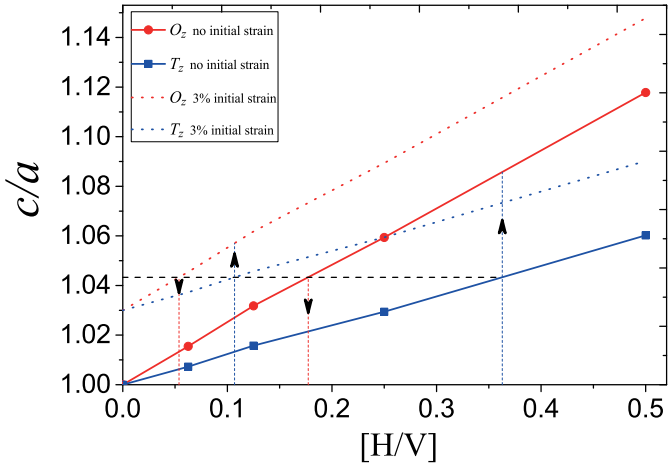

Figure 3.11. The uniaxial lattice strain c/a resulting from varying the concentration of hydrogen occupying exclusively either T_z sites (blue data points and lines) or O_z sites (red data points and lines) in *bcc* vanadium. The horizontal black dashed line at $c/a = 1.043$ marks the critical uniaxial lattice strain for which the hydrogen occupancy of T_z and O_z site becomes equal in energy, as seen in Figure 3.7. The vertical colored dashed lines indicate at which hydrogen concentration the critical c/a ratio of 1.043 is reached for occupancy of T_z ([H/V] = 0.363) and O_z ([H/V] = 0.177) sites, respectively, when there is no initial strain (i.e. $c/a = 1.00$ for [H/V]=0). The dotted lines represent the case of an initial strain of $c/a = 1.03$ before any hydrogen has entered the system. The critical c/a ratio is reached at [H/V] = 0.107 for T_z occupancy and 0.054 for O_z occupancy.

If we instead increase the hydrogen concentration, as explained in the previous sections, and relax the structure to the equilibrium volume, we expect to see similar changes to the potential landscape. Thus, as an approximation, we disregard the hydrogen-hydrogen interactions, i.e. we say that the energetics of the hydrogen atoms is independent of the concentration and that the critical c/a ratio remains unchanged at 1.043 no matter how many H atoms we load into our system.

Figure 3.11, taken from Paper I is the change in volume as a function of the hydrogen concentration. The horizontal dashed line is the critical c/a ratio for change in occupancy, taken from Figure 3.7. When the hydrogen-induced change to the c/a ratio reaches the critical value of 1.043, we predict a shift in site occupancy from T_z to O_z, indicated by the upward arrow in Figure 3.11. The shift in site occupancy is accompanied by a further increase of c/a since we go from isotropic hydrogen-induced local strains to strongly anisotropic strains (c.f. Figure 3.9). The z-component of the strain in the case of O_z site occupancy is very large and since we only allow volume expansion in the z-direction, we predict an increase in volume (and therefore in the c/a ratio)

after the shift in site occupancy is completed. The shift in occupancy is a self-amplified process: every hydrogen atom making the shift will contribute to the increase in volume, thus making the O_z sites more energetically favorable since we are moving towards larger c/a in Figure 3.7, which favors the O_z sites (β-phase) more than the T_z sites because of the steeper descent of the curve for the energetics of the O_z sites (see Figure 3.7). It will thus be easier for the following hydrogen atoms to make the shift in site occupancy. All hydrogen atoms will thus eventually occupy O_z sites and the resulting strain is $c/a = 1.102$. We thus have, in terms of strain, moved away from the critical value of 1.043.

If we start taking hydrogen out of our system, we will reduce the strain and again move towards the critical c/a value of 1.043. When we reach the critical c/a value, the site occupancy is shifted back to T_z. Again the shift is self-amplified since every single hydrogen that changes its site occupancy will induce a small decrease in the volume of the system which favors occupancy of T_z sites. The T_z to O_z and the O_z to T_z shifts in occupancy thus occur at different hydrogen concentrations [H/V], as indicated by the two vertical lines in Figure 3.11. We thus predict hysteresis in volume during loading and unloading of hydrogen in the constrained vanadium film. This phenomenon has been experimentally observed [22, 31].

3.3.3 Shift in site occupancy from energetics

Each data point in Figure 3.11 has been calculated from the average of 50 random hydrogen distributions, as explained in Section 3.2.4. Using the average energy for each of these data points and comparing the total energies of T_z and O_z occupancy as a function of hydrogen concentration, we can predict at what concentration the shift in site occupancy occurs. Results can be viewed in Figure 3.12. The horizontal dashed line at $c/a = 1.043$ in Figure 3.11 intersects the datasets of T_z and O_z at different concentrations [H/V]. But we know from Figure 3.7 that the energy of site occupancy at T_z and O_z are the same at the strain state corresponding to $c/a = 1.043$. Thus, at two different hydrogen concentrations, [H/V] = 0.363 and [H/V] = 0.177, the H atoms in the T_z sites and the O_z, respectively, will have the same energy of site occupancy. The two vertical dashed line indicate these concentrations. At these points we approximate that the activation energy of shift in site occupancy is near to zero and that the shift will, therefore, happen spontaneously (i.e. T_z to O_z at [H/V] = 0.363 and O_z to T_z at [H/V] = 0.177). The shifts can, however, occur anywhere between the two vertical lines since the H atoms then change their strain state to either suite occupancy at the O_z or T_z sites (i.e. the strain state of the system being either more or less than $c/a = 1.043$). But in the region between the vertical lines, the activation energy will be larger than 0. If we however only look at the energetics, there can be only one concentration [H/V] correspond-

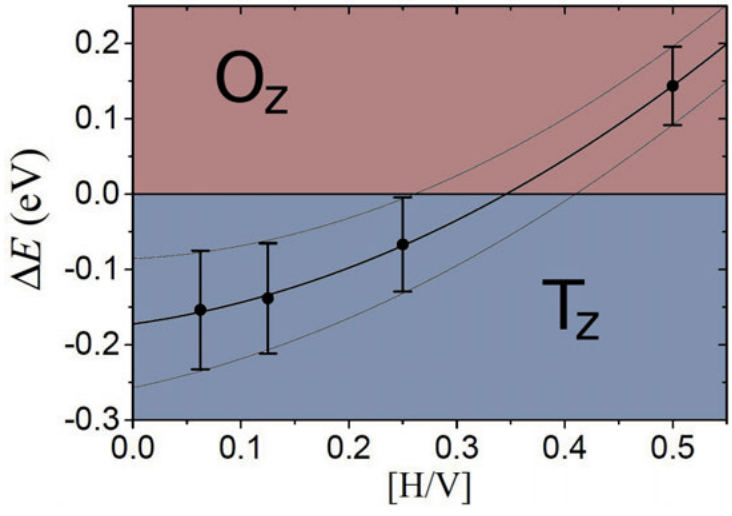

Figure 3.12. Energy difference between T_z and O_z occupancy at optimal c/a ratios as a function of hydrogen concentration. $\Delta E = (E_{T_z} - E_{O_z})/N_H$ where N_H is the number of hydrogen atoms in the simulation. Data points are for average values and the bars indicate $\pm$ one standard deviation (defined as the square root of the variance). Lines are second order polynomial fits.

ing to equality in total energy between having all H atoms either in T_z sites or O_z sites. This is the only concentration where a shift in site occupancy will not alter the total energy of the system. This occurs at [H/V]=0.34 (c.f. Figure 3.12).

3.4 Hydrogen diffusion

Fick formulated the law of diffusion in 1855, relating the diffusion-facilitated flux to the concentration gradient [51], referred to as chemical diffusion. Before that, the motion of very small grains had been observed on water, in the absence of any concentration gradients (or chemical potentials). This observation was explained by introducing the concept of very small entities that would later be termed atoms and molecules. The very small building blocks of water were believed to be interacting with the small grains and making them move by colliding with them. This type of motion is called Brownian motion, named after the botanist Robert Brown who discovered the phenomenon in 1827 (Ref. 52). In 1905, Albert Einstein explained the interaction of the water molecules with the small grains [53].

Diffusion of hydrogen in a metal lattice is atomistically described by the interaction between the hydrogen atoms and the metal atoms. Hydrogen in transition metals can be considered as an ideal system for studies of the rate

of diffusion, as the changes in electronic structure are small during diffusion events and because the diffusion obeys Arrhenius law at elevated temperatures [54].

There are different diffusion mechanisms that play important roles depending on the temperature region. In the low temperature region, the phonon-electron coupling is very weak so that the H atom can diffuse without changing the phonon state, this is referred to as coherent tunneling [2]. With increasing temperature, the phonon interaction increases and as a consequence, the probability of two neighboring sites being brought to energetic coincidence is increased. When the sites are level in energy, the H atom can diffuse between the sites in what is referred to as phonon-assisted tunneling [2]. If the temperature is increased further, the phonon-assistance can bring the H atom over the barrier (activation energy E_a) between the sites and we have classical diffusion. This is called the classical regime of diffusion [2].

Even though the forces acting on the atoms are calculated from quantum mechanics, no quantum mechanical effects are included in the Molecular Dynamics (MD) simulation throughout this Thesis. The atoms are treated as classical particles. Tunneling is not possible and the total energy of the particles does not contain any zero-point energy corrections. From the wave nature of particles, we know the importance of tunneling when talking about the motion of small particles in the low temperature regime. With hydrogen being the lightest atom, its corresponding de Broglie wavelength is the longest of all elements.

It is thus very important that the temperature is high enough so that classical diffusion is the dominant diffusion mechanism. The thermal energy of a particle at room temperature is 0.026 eV, as given by k_bT. Though the hydrogen activation energies are usually much larger than that (cf. 0.045 eV in α-phase vanadium [2]). In classical dynamics, for a hydrogen atom trapped in a frozen potential energy landscape, the hydrogen will never diffuse. Rather than the dynamics of the hydrogen itself, it is the dynamics of the potential energy landscape that is the key to understanding the diffusion of hydrogen in transition metals. For an adiabatic transition of hydrogen, the vibrational frequency of the atoms of the host lattice are the ones that play a crucial role. There is a correlation between the Debye frequency of the host lattice and the diffusion coefficient of the hydrogen atom as the frequency of attempted jumps made by the hydrogen is linked with the Debye frequency [2]. It is known that the diffusion coefficients of the isotopes H, D and T converge as the temperature is increased [2], the Debye frequency dependence on the diffusion is a probable explanation for this. Though if the temperature is increased beyond the melting temperature of the host lattice, the particles are no longer confined in potential wells and the atoms would undergo free motion like diffusion and we would thus expect the lighter isotope to diffuse the fastest. In the low temperature region, the mass of the isotopes is very important as tunneling is the dominant diffusion mechanism.

3.4.1 *Ab initio* Molecular Dynamics

We utilize *ab initio* quantum molecular dynamics to treat the thermal motions of atoms. The motions are governed by Newton's second law of motion

$$\mathbf{F}_I = M_I \ddot{\mathbf{R}}_I, \tag{3.2}$$

where $\mathbf{R}_I$ and $\mathbf{F}_I$ are the position and force on nuclei I with mass M_I. The double dots denote the second time derative, i.e. the acceleration.

The VASP code utilizes Born-Oppenheimer MD which allows for decoupling of the nuclei and the electrons. Likewise are the calculations decoupled because the electronic degrees of freedom are treated first with the nuclei kept frozen. The self-consistent Kohn-Sham equations are solved and the forces acting on the nuclei are calculated and their positions are updated accordingly, i.e. the optimization of the electronic structure and the movement of the nuclei are decoupled. The nuclei are usually referred to as moving on a Born-Oppenheimer potential energy surface.

Temperature is related to the energy via equipartition, where at thermal equilibrium, the energy is shared equally between all atoms. If not specified for each atom, the initial velocities and the resulting kinetic energy of the atoms, are assigned in a random manner according to the Maxwell-Boltzmann distribution, with the constraint that the center of mass of the system must be fixed.

The initial time steps of the simulation will result in unphysical energies of the system due to the random velocities that are given to the atoms. The initial time steps of the simulation must be used for equilibration and thus be discarded. The equilibration is one of the limiting factors of MD simulations, especially when the temperature is altered throughout the simulation. Depending on the complexity of the system, a significant amount of simulation time will be needed for equilibration.

For simplicity, it is common to look at a global property of the system, such as the total energy or pressure to avoid calculating an ensemble average. Apart from the volume and number of particles, which are usually kept fixed along with the temperature (canonical NVT ensemble), we can choose any global property. The stability of this property over time will tell us whether or not the system is equilibrated.

Figure 3.13 shows the total energy with respect to time for an MD simulation of hydrogen in vanadium. The total energy can initially be seen to fluctuate a lot as compared to the later part of the simulation. The red curve is produced by applying a fast Fourier transform (FFT) filter to the signal. The horizontal line is the average total energy of the later equilibrated part of the simulation. It is clear that one should at least discard the first couple of thousands fs of the simulation. In all our MD simulations of hydrogen in vanadium, we consistently discarded the first 10000 fs of data in each set.

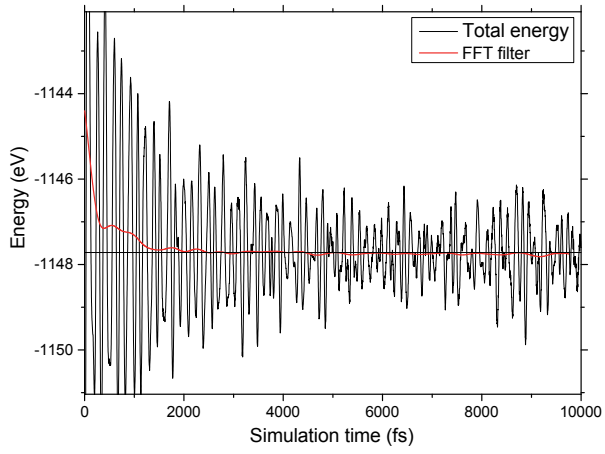

Figure 3.13. Equilibration of MD simulation of hydrogen in vanadium.

3.4.2 Jump-angle distribution

One way of describing the direction of diffusion in a lattice gas model is to calculate the jump-angle distribution (JAD) [55]. The jump-angle is defined as the angle between two consecutive jumps, e.g. two jumps in the same direction constitutes a 0° jump-angle, while jumping back and forth constitutes a 180° jump-angle, and so forth.

If we consider the nearest T-T neighbors as the longest allowed jumps, while also including O sites, there is a total of 6 possible jump-angles in the *bcc* lattice. The possible jump-angles are illustrated in Figure 3.14.

All jumps during the MD simulation are counted and normalized to one to give a probability distribution of the various types of occurring jump-angles. In a completely random jump model, all jumps have equal probability. It is when we introduce some constriction on the diffusion that we see a partitioning of the jump-angles. A general assumption that one can make regarding the interpretation of the JAD is that a preference for a certain jump-angle (or a few jump-angles) means a high level of constriction on the diffusion. If the distribution is shifted towards low jump-angles we have in the general case quicker diffusion than if the jump-angles are high.

3.4.3 Effect of biaxial tensile strain on diffusion of hydrogen in vanadium

The high ductility of vanadium allows the material to tolerate high strain before structural deformations are formed such that the structure is no longer monocrystalline body center tetragonal. Along with its good kinetics of diffu-

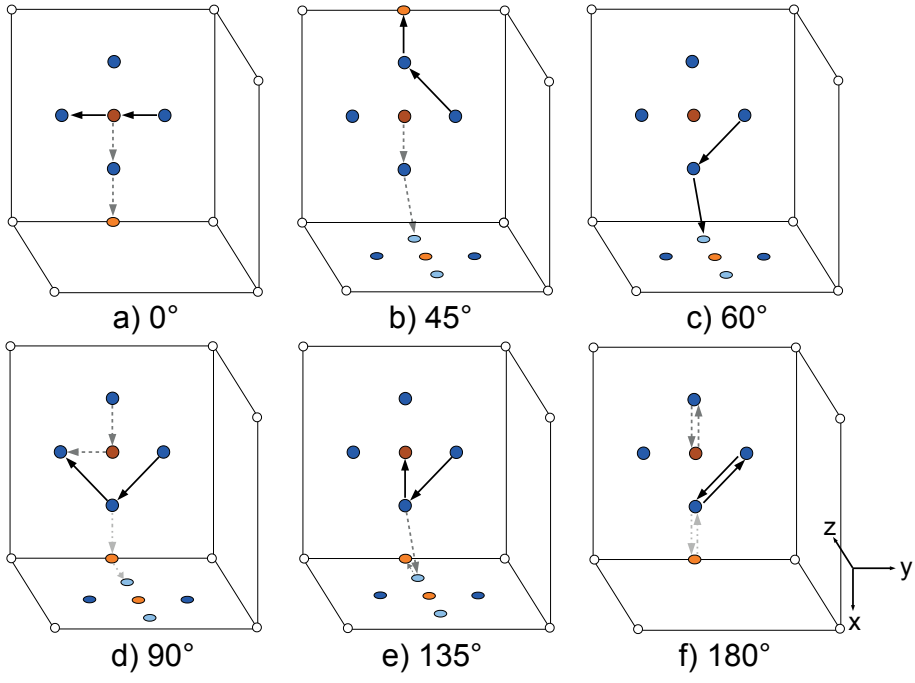

Figure 3.14. Possible jump-angles between interstitial sites in a bcc lattice.

sion [54] these properties make vanadium well suitable for studies of strain-induced metal-hydrogen properties.

We have studied the diffusion of hydrogen in vanadium using *ab initio* molecular dynamics (MD) simulations. The aim is to explore the difference in diffusion between the α and β-phase configurations with a focus on diffusion paths and diffusion coefficients. What is studied is the self-diffusion (or tracer-diffusion) of the hydrogen as it jumps between interstitial sites in the metal lattice. Self-diffusion of the hydrogen means that the diffusion in not caused by a chemical potential. The diffusion coefficients D are calculated using the formula of interstitial lattice diffusion derived from the *Chudley-Elliot* model [56] and is given by

$$D = \frac{d^2}{6\tau}, \tag{3.3}$$

where d is the distance between interstitial sites and τ is the mean residence time.

In the body-centered tetragonal (*bct*) structure there are three types of tetrahedral sites and three types of octahedral sites that originate from being oriented in different directions with respect to the direction that the lattice is strained along (see Figure 3.2). From experiments, the preferred site occupancy of hydrogen in vanadium has been determined to be interstitial tetra-

hedral sites in the α phase [31]. As discussed earlier, the preferred site occupancy of hydrogen is known to be linked to the strain state of the structure [23, 24, 31, 32, 40, 41]. When vanadium is subjected to tensile strain, the preferred site occupancy will shift from tetrahedral to octahedral [23, 24, 31, 32, 40, 41] (β-phase configuration). Biaxial compressive strain is applied in the x- and y-directions which result in a tensile strain in the z-direction due to the Poisson response. The strain in the x- and y-directions are of the same magnitude, this will render the T_x and T_y sites identical and the same is true for the O_x and O_y sites. The x and y-sites are identical except for a 90° rotation around the z-axis. We will, therefore, use the mutual notations T_{xy} and O_{xy}. In the case of no strain (i.e. $c/a = 1.00$), there is no distinction and in most of the literature, the sites are denoted T and O.

When we investigated the effect of **uniaxial** strain on the energetics of hydrogen in vanadium in Paper I, we found that energy of a self-trapped hydrogen atom at the T_z and O_z sites at the strain state around $c/a = 1.05$ are equal. We therefore deemed it interesting to investigate the diffusive properties at that strain state. As a reference, we also investigated the diffusive properties for the case of no strain (i.e. $c/a = 1.00$), in which, the system is known to be in the α-phase (T-site occupancy) and the diffusion coefficients have been measured experimentally in many studies. To also investigate the low concentration β-phase configuration (O_z-site occupancy), we chose a strain state of $c/a = 1.10$ where we expect a considerable energetic preference for O_z-site occupancy. Furthermore, the strain state of the β phase in bulk $VH_{0.5}$ is close to $c/a = 1.10$ (Ref. 2). We can thus make qualitative comparisons between experimental findings in the $VH_{0.5}$ hydride with our results in the same strain state but in the low concentration region.

In Paper I the **uniaxial** tensile strain was achieved by keeping the supercell fixed in the xy-plane and we either varied the strain in the z-direction manually while keeping the hydrogen concentration fixed or by increasing the hydrogen concentration and performing constrained cell relaxation in the z-direction. In Paper II we instead investigated the effect of **biaxial** tensile strain by contracting the supercell in the x and y directions and then performing constrained cell relaxation in the z-direction. Several values for $x = y$ were tested until the subsequent Poisson response in the z-direction yielded the desired strain states of $c/a = 1.05$ and 1.10.

Figure 3.15 shows the potential energy surfaces (PES) for the strain states of $c/a = 1.00$, 1.05 and 1.10. The small spheres indicate the positions of the interstitial sites on a (100) surface with the color coding following the same pattern as those in Figure 3.2. The hydrogen atom was first relaxed into a self-trapped state in the vanadium supercell, then the vanadium atoms were held fixed in those positions while we mapped the PES by calculating the energy for several positions of the hydrogen atom on a square grid on the (100) surface. That is, we are mapping the landscape of the self-trapped hydrogen atom (cf. dashed line in Figure 3.5). The total energy in the initial simulation of the

self-trapped hydrogen atom is set to 0 eV, i.e. the energy scale is such that the numbers on the energy axis show the increase (or decrease) in energy required to move the hydrogen atom on the (100) surface. For $c/a = 1.00$, the PES clearly shows the expected energetic favorability of T-site occupancy and the saddle point that is the most probable $T \rightarrow T$ diffusion path. At $c/a = 1.05$, the PES looks quite flat in and around the O_z site and we can also see that there is now a clear distinction between the O_z and O_{xy} sites, with the latter being substantially higher in energy. The flatness of the PES at $c/a = 1.05$ is also expected based on the experimentally observed decrease in zero-point energy in the β-phase as compared to the α-phase [2], which is also investigated by us in Paper III. In our earlier work on uniaxially strained vanadium in Paper I we found that the T_z and O_z sites were near equal in energy at the strain state of $c/a = 1.05$ in the case of comparing the cases of the hydrogen being self-trapped in either site. In the current case of biaxial strain at $c/a = 1.05$, there is a 0.29 eV difference in energy between the T_z and O_z sites when comparing the energy of the positions of the red and blue spheres in Figure 3.15 at $c/a = 1.05$. This is however from static calculations at 0K where no dynamical effects can interfere with the self-trapping of the hydrogen atom. The strains imposed on the constituent atoms of the T_z and O_z sites from accommodating a hydrogen atom was investigated in Paper I. It is however not only the hydrogen atom that diffuses, the strain field also diffuses together with the hydrogen as a quasiparticle. The bound state of the hydrogen and its accompanying strain field is usually referred to as the polaron picture [2, 57]. The PES only provides us with a piece of the puzzle when it comes to the understanding of diffusion of hydrogen in vanadium, or more generally, the diffusion of a lattice gas.

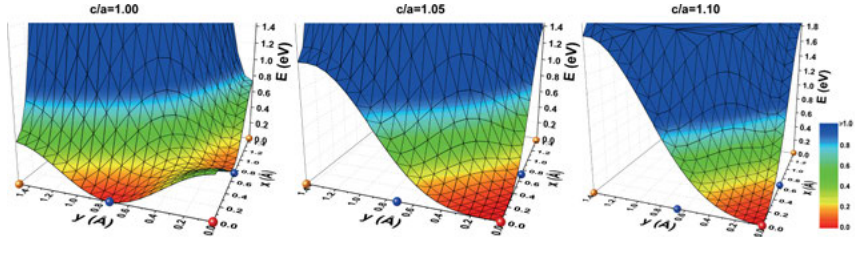

Figure 3.15. Potential energy surfaces of hydrogen in vanadium.

To investigate the hydrogen distribution in the 4 unique sites (T_z,T_{xy},O_z and O_{xy}) over time in the MD simulations, we have in Figure 3.16 plotted isosurfaces of the distribution. The 4×4×4 bcc cells are mapped onto one bcc unit-cell. The iso-surfaces are 3-dimensional histograms that are cut in the [100] planes of the bcc unit cell. The arbitrary units of hydrogen density increase from blue to red.

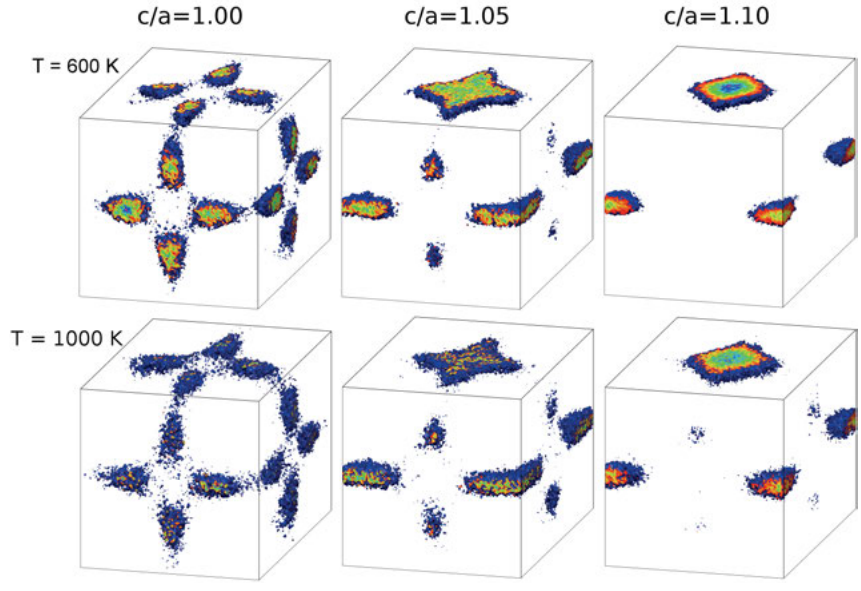

Figure 3.16. Isosurfaces of the hydrogen distribution. Density increases from blue to red.

The hydrogen distribution in the MD simulations at $c/a = 1.00$ is in agreement with the known T site occupancy (cf. Figure 3.2) in bulk vanadium in the α phase [2]. From the PES we established that the O_z sites are "open" for hydrogen occupation as the energy minimum is at (or in the vicinity) of the O_z sites and that the confinement of the hydrogen atom is increased as the tensile strain increases. In the isosurfaces, we can see the same trend.

When comparing the isosurfaces for 600 K and 1000 K, the main difference is that the results for 1000 K are less well defined. With the increased temperature the atoms have higher kinetic energy which in turn means that they can be displaced further from their respective equilibrium positions. Hence we have more yellow and red on the isosurfaces at 600 K than at 1000 K because of stronger localization of the hydrogen atom at a lower temperature.

At $c/a = 1.10$ it is apparent from the isosurfaces that the exact geometrical positions of the O_z sites are not the most stable as the center is blue and thus in the low end of the spectra while a red region can be seen around the O_z site which indicates high density. From studying the pair distribution function given by X-ray and neutron diffraction data for β-V_2D, Itoh and Fukunaga found that the D atoms are displaced 0.08(2) Å away from the O_z centers [58]. Our corresponding results for β phase configuration in a diluted V-H system for $c/a = 1.10$ are 0.134 Å at 600 K and 0.198 Å at 1000 K, calculated from the radial distribution in the [001] plane with respect to the geometrical center of the O_z site. The radial distribution can be seen in Figure 3.17.

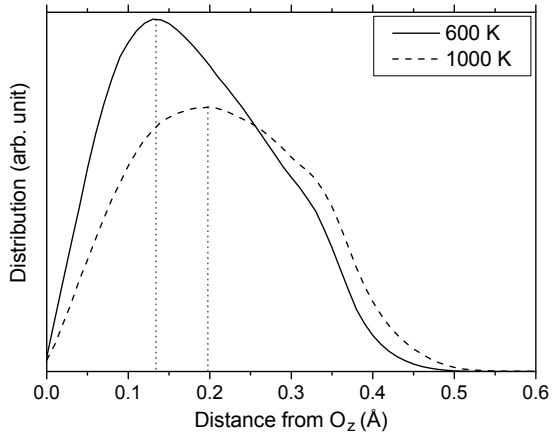

Figure 3.17. Radial distribution of the H atom trapped in a O_z site at $c/a = 1.10$. The vertical lines indicate the peak positions.

Table 3.2 shows the calculated diffusion coefficients D and experimental values D_{exp}. The last column represents the average nearest V-H distance. The 600 K data for $c/a = 1.10$ was omitted because insufficient hydrogen jumps were recorded during the simulation to give a statistically valid result. We can see a substantial drop in diffusivity with strain. In Paper IV, the experimental ratio of diffusion when comparing the α and β phase configurations in the low concentration limit, D_α/D_β, is found to be in the range of 3 to 5, depending on the temperature ($\sim$400–500 K). From the MD simulation, the smallest ratio is given by $D_{1.00}/D_{1.05}$ at 1000 K, it is 1.58. The largest ratio is given by $D_{1.00}/D_{1.10}$ at 1000 K, it is 4.95. The ratio is obviously very dependent on the strain state. The exact strain state of the V film in the experiments is not known but believed to be close to 3% [23], thus we have a large mismatch in strain and can only ascertain the qualitative agreement that tensile strain slows down diffusion. "...a dramatic difference in the rate of hydrogen diffusion in the two phases..." were the words J.M Rowe *et al.* used to described the change in the rate of diffusion before and after crossing the α to β phase-boundary for the $VH_{0.570}$ hydride [59]. From nuclear magnetic resonance (NRM) measurements, they found an approximated activation energy of 0.155 eV. Asano *et al.* reported an activation energy of 0.266 eV from NMR measurements on β-phase $VH_{0.68}$ [60]. In Paper IV we experimentally obtained an activation energy of 0.217(17) in the low concentration limit. Utilizing Arrhenius law and the diffusion coefficients at 600 K and 1000 K for $c/a = 1.05$, an activation energy of 0.252 eV is obtained from our MD simulations.

We know that when tensile strain is applied, the preferred site occupancy is shifted more and more from T sites to O_z sites and that the movement in the *xy*-plane becomes restricted (see Figure 3.15). To investigate the diffusion

Table 3.2. *Diffusion coefficients calculated from mean residence time τ or, correspondingly, the jump rate $1/\tau$ and the average jump-length d (see Eq. 3.3).*

c/a	D [cm^2/s]	D$_{exp}$[cm^2/s]	Mean H-V dist [Å]
		Temperature: 600 K	
1.00	9.00×10^{-5}	$13.2\pm3.5 \times 10^{-5}$[61]	1.6694
1.05	1.85×10^{-5}		1.6600
1.10	-		1.6926
		Temperature: 1000 K	
1.00	20.5×10^{-5}	$18.6\pm4.4 \times 10^{-5}$[61]	1.6504
1.05	13.0×10^{-5}		1.6384
1.10	4.14×10^{-5}		1.6574

path, we study the jump-angle distribution (JAD) (Figure 3.18) and we also record all jumps to calculate the fractions of jumps from any type of site to any other type of site which is given in Table 3.3.

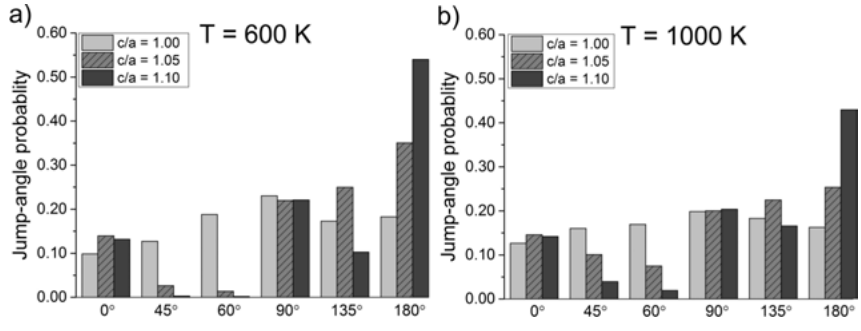

Figure 3.18. Probability of the angle between two consecutive jumps of the H atom at, a) T=600 K and b) T=1000 K for $c/a = 1.00$, 1.05 and 1.10.

Two of the more distinct features of the JAD when altering the strain state are the increase in 180° jumps and the decrease in the 45° and 60° jumps. We know from previous studies that the preferred site occupancy is shifted from T to O_z when tensile strain is applied and that movement in the xy-plane becomes restricted. It is reasonable to ask how the hydrogen moves between the O_z sites, or correspondingly, how hydrogen breaks out of the $4T_z$+O_z sites. We still maintain the geometrical T and O centers as the site positions despite of changes to the PES with strain. We know that the O_{xy} sites are energetically very unfavorable (cf. Figure 3.15) so it is a very unlikely diffusion path. The only two jump angles that break the hydrogen out of the $4T_z$+O_z sites without interaction with the O_{xy} sites are 0° and 45°. These jumps include interaction with the T_{xy} sites and from Table 3.3 we can see that for $c/a = 1.05$ and 1.10 that the $T_z \leftrightarrow T_{xy}$ jumps play a big role in the diffusion when also considering

Table 3.3. *Fractions of H-jumps between any of the four interstitial sites T_z, T_{xy}, O_z or O_{xy}.*

	Temperature: 600 K			Temperature: 1000 K		
Int. sites	$c/a = 1.00$	$c/a = 1.05$	$c/a = 1.10$	$c/a = 1.00$	$c/a = 1.05$	$c/a = 1.10$
$T_z \leftrightarrow T_z$	0.214	0.202	0.059	0.186	0.206	0.119
$T_z \leftrightarrow T_{xy}$	0.373	0.036	0.007	0.323	0.144	0.049
$T_z \leftrightarrow O_z$	0.148	0.750	0.934	0.158	0.528	0.800
$T_z \leftrightarrow O_{xy}$	0.135	0.005	0.000	0.161	0.057	0.012
$T_{xy} \leftrightarrow T_{xy}$	0.007	0.000	0.000	0.012	0.004	0.000
$T_{xy} \leftrightarrow O_z$	0.002	0.000	0.001	0.008	0.009	0.010
$T_{xy} \leftrightarrow O_{xy}$	0.121	0.006	0.000	0.148	0.049	0.010
$O_z \leftrightarrow O_z$	0.000	0.000	0.000	0.000	0.000	0.000
$O_z \leftrightarrow O_{xy}$	0.000	0.000	0.000	0.004	0.003	0.000
$O_{xy} \leftrightarrow O_{xy}$	0.000	0.000	0.000	0.002	0.000	0.000

that the high probability jumps $T_z \leftrightarrow T_z$ and $T_z \leftrightarrow O_z$ are contained in the $4T_z$+O_z site. It is also worth noting that no direct $O_z \leftrightarrow O_z$ jump was recorded during the MD simulations.

The conclusion about diffusion in the β phase configuration is a significant drop in diffusion coefficient that depends on the temperature and strain state. Up to a critical point, the biaxial tensile strain increases the confinement of the hydrogen atom to the $4T_z$+O_z sites. The T_{xy} sites are the main mediators of diffusion in the β phase configuration.

4. Zintl phase hydride

In the previous chapter, we investigated the transition metal-hydrogen systems of V-H and $ScZr(NiCo)_2$-H in which the hydrogen is, predominantly, bound to the metal via metallic bonds that allow for varying compositions of hydrogen in interstitial sites. The Zintl phase hydrides are composed of an electropositive metal, such as the alkaline metals, alkaline earth metals or rare earth (RE) metals and an electronegative p-block metal. For the most part, hydrides formed with an s-block element are of ionic type and hydrides formed with p-block metals are covalent.

The Zintl phase materials investigated by us in Papers VI,VII are $NdGaH_x$ and $GdGaH_x$, respectively. These materials, and Zintl phase hydrides in general, do not offer good volumetric or gravimetric storage properties of hydrogen. For hydrogen storage applications, Zintl phase hydrides are not the best candidates. What these materials instead offer us are opportunities to study the fundamental properties of hydrogen induced changes to the structure and physical properties as they are known to dramatically change with the absorption of hydrogen [4, 5, 62].

The theoretical part of the studies are based on DFT as implemented in the Vienna *ab intio* simulation package (VASP). Structural optimization can offer great insight into the hydrogen induced effect on the structural properties. Studying the local and projected density of states and charge distribution of the atoms of the optimized electronic structure can we get information about the bonding. We also calculate the enthalpy of formation for several hydrogen concentrations to determine the stability of the hydrides. Testing several concentrations is motivated for Zintl phase hydrides as, during hydrogenation, intermediate phases are often observed when varying the hydrogen gas pressure and temperature. In Zintl phase hydrides, the formation energies for hydrogen occupation at different sites can differ a great deal because of the local electronic environments at the sites.

4.1 Computational setup

For NdGa and GaGd in Papers VI and VII, respectively, the CrB type structure visualized in Figure 4.1 was used. A $21\times7\times27$ Monkhorst-Pack [63] k-point mesh was employed to sample the Brillouin zone. For calculations of partial occupancy of the H1 sites, which are presented as blue dots in Figure 4.1, a supercell was created by a threefold expansion of the CrB unit cell in the

x-direction. For calculations on the supercell, the k-point mesh was reduced to 7×7×27. The H_2 molecule was calculated in a 8×8×8 Å box with Γ-point sampling of the Brillouin zone. For the $REGaH_x$ calculations, the kinetic energy cutoff for the plane waves was set to 600 eV. The electronic structure, exchange and correlation and the relaxation of the nuclei are treated in the same way as described in Section 3.1.

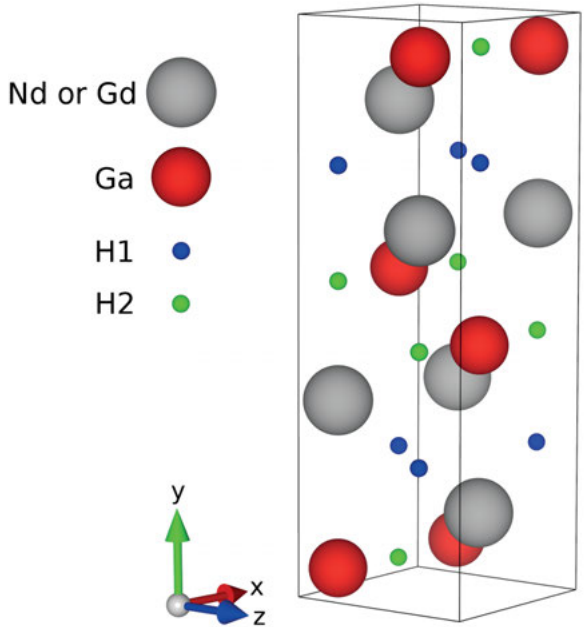

Figure 4.1. CrB type structure of NdGa and GdGa. The green and blue dots indicate the H1 and H2 positions.

4.2 Bonding

The theoretical side of the investigations on the Zintl phase hydrides is, to a large extent, aimed at describing the bonding of the hydrogen atoms to the p-block metal Ga and the rare earth metals Nd and Gd to provide a description of how hydrogen affects the electronic and atomic structures. The difference in electronegativity between the constituents makes the Zintl phase hydrides particularly interesting to study because of the intricate bonds that occur.

As a first approximation, we can look at the differences in the tabulated values of electronegativity of the constituents, which is, especially for a binary hydride, a good indicator of the bonding type. If there is a big difference in electronegativity we expect ionic nature of the bond and if the electronegativ-

ities are near equal then we expect predominantly covalent bonding [49]. Ga is close to H in electronegativity while Nd and Gd are much lower.

Hybridized electronic orbitals when comparing the site projected density of states of the H atoms electron with the valence electrons of the other constituent atoms indicates covalent bonding. From the *spd* decomposed density of states can we get information about which electrons are involved in the bonding and also the type of bonding, e.g. σ or π bonds.

We can determine the ionicity of the bonding by studying the charge transfer between atoms.

4.3 Bader charge analysis

We have utilized Bader charge analysis to calculate the atomic charges [64, 65]. The charge is calculated by integration of the charge density of the "Bader volume" of the atoms. The Bader volume is the volume of charge that belongs to an atom. To properly treat the Bader volume is the most crucial step of the Bader charge analysis. In Bader charge analysis this is, as the default setting, done by identifying the zero-flux surface of the charge density around each atom, i.e. $\nabla\rho(\mathbf{r})\cdot\hat{n}=0$.

In Papers VI and VII, the charges are given in units of the elementary charge e.

4.4 Results and discussion

From experiments during hydrogenation, intermediate phases are observed for both $NdGaH_x$ and $GdGaH_x$ for $0\leq x\leq 2$. Calculations of stability of hydrogen occupation at the H1 and H2 sites (see Figure 4.1) revealed that the enthalpy of formation of the two formations REGa + $(1/2)H_2$ = REGaH1 and REGa + $(1/2)H_2$ = REGaH2, that H1 occupancy is 0.41 and 0.43 eV more energetically favorable over H2 occupancy for NdGaH and GdGaH, respectively per formula unit REGaH. Thus, the H1 positions are filled first during hydrogenation in both $NdGaH_x$ and $GdGaH_x$. The H1 sites are of a tetrahedral shape and formed by the RE metals in the two compounds (i.e. Nd or Gd), while the H2 sites are coordinated by 2 Ga atoms and 3 RE atoms in a trigonal bipyramidal formation. The appearances of the H1 and H2 sites are presented more clearly in Figure 4.2. The blue H2 marker is positioned at the geometrical center of the trigonal bipyramidal site. We did, however, discover that the center positions was metastable and that the energy was lowered by 0.01 eV per formula unit by shifting the H atom towards either of the Ga atoms and thus reducing the symmetry. For $NdGaH_{1+x}$ the H atoms in the trigonal bipyramidal sites are relaxed to a distance of 1.8 Å and 2.4 Å to the Ga atoms on either side (red

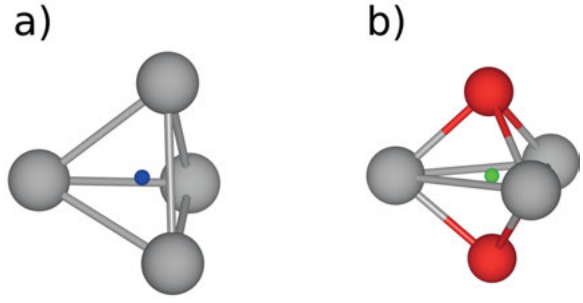

Figure 4.2. Visualization of, (a) tetrahedral and (b) trigonal bipyramidal of the CrB structure.

Ga atoms in Figure 4.2) and 1.9 Å and 2.3 Å for $GdGaH_{1+x}$ which indicates covalent Ga-H bonding.

For partial occupancy of the H2 sites, all the H1 sites were first filled and then H atoms were randomly distributed into the H2 sites of the $3\times1\times1$ supercell of the CrB structure. Several calculations of random hydrogen distributions were performed until the average total energies and structural parameters were converged (cf. Section 3.2.4) for $REGaH_{1.33}$, $REGaH_{1.66}$ and $REGaH_2$.

Figure 4.3 shows the heat of formation calculated according to

$$\Delta E = \frac{1}{1+x}\left[E(REGaH_{1+x}) - (E(REGa) + \frac{1+x}{2}E(H_2))\right] \qquad (4.1)$$

for $0\leq x\leq 1$. E denotes the total energy of the enclosed-in-brackets system. The red bars indicates $\pm$ the standard deviation from sampling several hydrogen distributions in the trigonal bipyramidal sites. The blue dots indicates the lowest energy distribution found. From the heat of formation, we can see that $NdGaH_x$ is slightly more stable but that the general trends for $NdGaH_x$ and $GdGaH_x$ are very similar.

The structural parameters from experiments are well reproduced by DFT and presented in Table 4.1.

When filling the tetrahedral sites and thus forming REGaH1, the lattice parameter a decreases and b increases while c remains essentially the same after hydrogenation. The incorporation of hydrogen only has a very small effect on the total volume.

Simple models of approximating the electronic "imbalance" can give us an idea of how many hydrogen atoms per formula unit the structure will want to hold to compensate for this imbalance. The number of nearest neighbors, considering a bond to each neighbor, and the number of valence electrons available for bonding will give us an idea of the imbalance. Hydrogen has a large electronegativity and will thus attract electrons. Negatively charged hydrogen is referred to as being in a hydridic state. The introduction of hydrogen

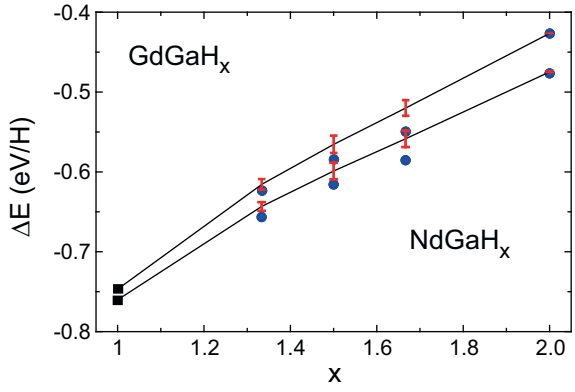

Figure 4.3. Heat of formation for $NdGaH_x$ and $GdGaH_x$ for $1 \leq x \leq 2$.

Table 4.1. *Lattice parameters of CrB structure from DFT and experiments.*

	DFT			Experiments		
Int. sites	$c/a = 1.00$	$c/a = 1.05$	$c/a = 1.10$	$c/a = 1.00$	$c/a = 1.05$	$c/a = 1.10$
NdGa	4.4625	11.3735	4.1885	4.4306(3)	11.2478(8)	4.1806(3)
NdGaH	4.2211	12.0192	4.2013			
$NdGaH_{1.33}$	4.1801	12.1142	4.2009			
$NdGaH_{1.50}$	4.1750	12.1488	4.1968			
$NdGaH_{1.66}$	4.1796	12.1703	4.1903	4.1103(7)	12.253(2)	4.1665(8)
$NdGaH_{2.00}$	4.2125	12.2074	4.1800			
GdGa	4.3891	11.0250	4.0970	4.340(3)	11.012(2)	4.105(3)
GdGaH	4.0728	11.6885	4.1199			
$GdGaH_{1.33}$	4.0346	11.8071	4.1105			
$GdGaH_{1.50}$	4.0298	11.9021	4.1022			
$GdGaH_{1.66}$	4.0270	12.0092	4.0906	3.9867(7)	12.024(2)	4.1009(6)
$GdGaH_{2.00}$	4.1023	11.8529	4.0834			

in these type of materials is thus very likely to have a large influence on the electronic structures as new covalent and ionic bonds are formed.

Table 4.2 shows the calculated Bader charges. The trends for $NdGaH_x$ and $GdGaH_x$ are very similar. As expected, the more electronegative p-block metal Ga carries a negative charge. When filling the H1 sites, both the RE and the Ga atoms contribute to the charge of the hydrogen atoms. When filling the H2 sites, it is evident that there is a H2-Ga bond, as, almost all charge transfer is from the Ga atoms to the hydrogen atoms in the H2 positions while the charges of the H1 hydrogen atoms and the Nd atoms remain essentially the same.

Figure 4.4 shows the density of states (DOS) for $NdGaH_x$ for x=0, 1 and 2 with partial contributions of Ga, H1 and H2 in (a) and partial contributions of Ga p_x, Ga $p_y + p_z$ in (b). The Fermi level is set to 0 eV and is indicated by horizontal lines in the top figures. Filling the H1 tetrahedral sites and thus forming NdGaH has only a small effect on the electronic structure. With the hydrogen atoms in the tetrahedral sites being coordinated by Nd atoms, no di-

Table 4.2. *Calculated Bader charges in units of the elementary charge e.*

	Nd	Ga	H1	H2
NdGa	1.0394	-1.0394		
NdGaH	1.4589	−0.7929	−0.6659	
$NdGaH_2$	1.5390	−0.3789	−0.6461	−0.5139
	Gd	Ga	H1	H2
GdGa	1.3604	-1.3604		
GdGaH	1.5402	-0.8467	-0.6935	
$GdGaH_2$	1.6205	-0.4094	-0.6784	-0.5326

rect hybridization with the Ga atoms is to be expected and thus the partial Ga DOS can be seen to remain essentially unchanged. The DOS at Fermi level changes considerably when going from NdGa to NdGaH and from NdGaH to $NdGaH_2$ as a pseudogap can be seen to form. This is expected when the electron imbalance has been mended by the introduction of hydrogen as more states are made available at lower energies. The contribution of the H1 and H2 hydrogen atoms to the DOS are very different. For H1 we can see a narrow peak and thus only weak dispersion. This means that the bond is predominantly of ionic type and that the hydrogen is hydridic. The contribution of H2 hydrogen to the DOS is clearly very different. In the lower plots where we show the partial contributions of Ga p_x, Ga $p_y + p_z$ and H2. The partial distribution of H2 is spread over a large energy and is essentially mirrored by the partial distribution of Ga. It is evident that H2 bonds are of covalent character, as opposed to the more ionic nature of the H1 bonds. The Ga p_x contribution is heavily affected by the introduction of H2 hydrogen atoms and we thus conclude, as one would expect from the symmetry considerations, that the H2 hydrogen is carried by a bond to the Ga p_x orbital as the –Ga–H2–Ga–H2– chains run in the x-direction.

The total DOS for GdGa, GdGaH and $GdGaH_2$ are shown in Figure 4.5. The DOS for $NdGaH_x$ and $GdGaH_x$ exhibit very similar electronic structures.

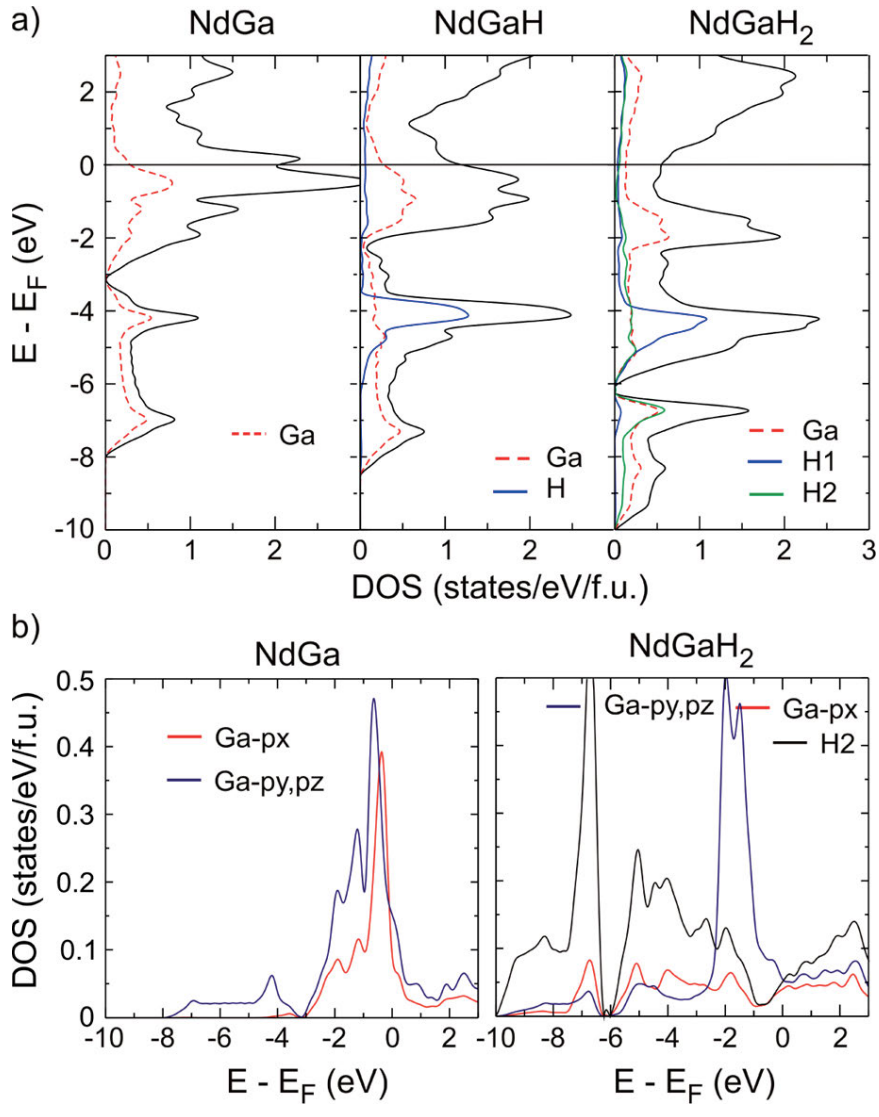

Figure 4.4. (a) Electronic density of states (DOS) for NdGa, NdGaH, and $NdGaH_2$ with partial contributions of Ga, H1, and H2. (b) Partial DOS for Ga p_x,Ga p_y+p_z, and H2 for NdGa and $NdGaH_2$

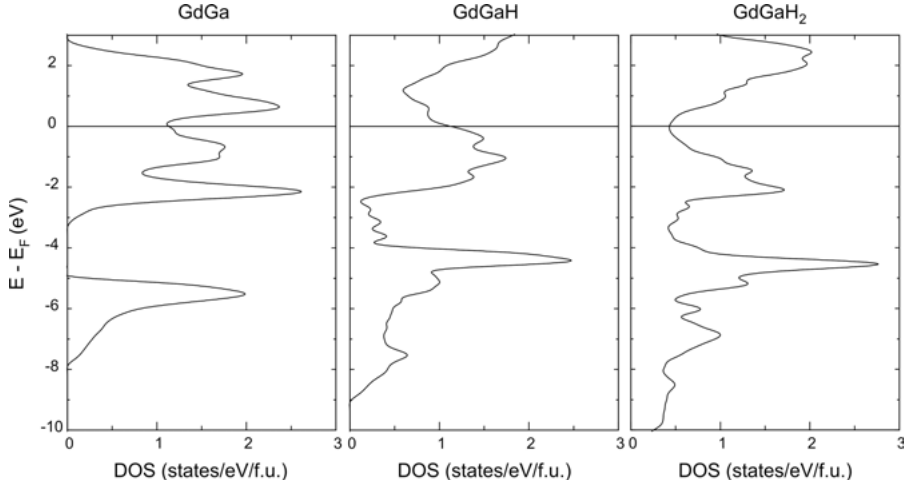

Figure 4.5. Total electronic density of states (DOS) for GdGa, GdGaH, and $GdGaH_2$

5. Amorphous Iron-Zirconium

An amorphous material is a solid material in a structurally nonstable equilibrium. The structure of an amorphous material is defined by short-range order and long range disorder [3]. It has been known for a long time that quenching (heating and rapid cooling) a material has, most notably, significant effect on the mechanical properties of the material, such as hardening and protection against corrosion [66, 67]. A disordered material has the ability to better dissipate energy through spreading out the shear and strain in the material [66, 68]. The resistance to corrosion is believed to partly stem from the absence of grain boundaries and dislocations in amorphous materials. More recently the magnetic properties of amorphous materials have caught the attention of many researchers [69]. The structure, interatomic distances and coordination numbers can be altered through quenching, alloying and implantation of smaller atoms. This will affect the exchange interaction between the atoms and consequently also the magnetic properties of the material. Amorphous materials thus have a large range of applications that makes them interesting for the industry.

There are many studies on amorphous materials where a theory for sphere packing has been employed to predict the structural properties [70–74]. These studies range from very simple models, e.g. Vegard's law [75], which works fairly well for many alloys as a first order approximation to more advanced mathematical models. The highest packing fraction of identical spheres is that of a close packed structure (hcp or fcc) which has a packing fraction of 0.74. When packing spheres of different radii, higher packing fractions can be achieved. In the case of two different types of spheres, the highest packing fraction is achieved when the larger type of sphere occupies 70 to 80% of the total volume, regardless of the relative volume of the spheres [71]. The packing fraction increases when the relative volume increases. The packing fraction of a random closed packed structure is 0.64 and that number has been produced in a large variety of experiments and simulations [3, 70]. Making the assumption that an amorphous structure can be approximated with a close random packed structure and using the atomic volumes of the atoms in their respective crystalline phases, we can estimate the density of our binary amorphous material to what we expect to be in qualitative agreement with the real samples. We are employing density functional calculations to investigate the structure of amorphous FeZr. The computational details of the simulations are explained in Section 5.1. Due to the high computational cost of a full volume relaxation, we expected computationally heavy calculations because of the required number of atoms that needs to be included. Under that premise,

we decided to not perform volume relaxation of the investigated compositions of FeZr and instead opted to use set densities. Test calculations of different densities given by both empirical data and sphere packing models showed that the ratio of the peak positions of the radial distribution function (RDF) remained essentially the same. The short-range order that we define by Voronoi polyhedra also remained essentially the same for the tested densities. We are therefore not concerned with the absolute changes in interatomic distances, as they do of course change with density. They do however scale with the volume for the tested densities which is another way of saying that the relative peak positions do not change. We do instead focus on the evolution of the relative peak positions of the RDF and the Voronoi polyhedra when we alter the $Fe_{1-x}Zr_x$ composition.

What all computational modelling of amorphous materials has in common is the requirement to include sufficiently many atoms so that the long-range disorder can be modeled. Long-range disorder means that the RDF is essentially flat and equal to one if normalized with respect to an ideal gas. The most common way to model disordered systems is by rapid quenching in molecular dynamics simulations [76–78]. As explained earlier, molecular dynamics simulations are computationally very heavy. Usually, the material is equilibrated at some elevated temperature above the melting point and then rapidly cooled (quenching). The computational cost to mimic the experimental cooling rates is very expensive. The computational cooling rates are usually of the order of 10^{12} K/s, while in experiments, the corresponding number is of the order of 10^7 K/s. In our work on amorphous FeZr in Paper VIII we have instead adopted the less heavy stochastic quenching method which can be seen as a shortcut when generating amorphous structures as compared to MD simulations [6–8]. Details on the stochastic quenching method are given in Section 5.2.

5.1 Computational setup

Supercells consisting of 200 atoms were used to model the amorphous FeZr structures. A minimum of 50 structures was simulated for each investigated FeZr composition to ensure that the average total energy of the structures was converged (cf. Section 3.2.4). The Γ-point alone was used to sample the Brillouin zone. The electronic structure, exchange and correlation and the relaxation of the nuclei are treated in the same way as described in Sections 3.1 and 4.1.

5.2 Stochastic Quenching

An alternative to the computationally heavy temperature equilibration in MD simulations is the relaxation of stochastic atomic configurations to a near energy minimum on the potential energy landscape [6–8]. The only constraint in the creation of the stochastic configurations is the minimum allowed distance between nearest neighboring atoms. One of the main reason for this is to avoid numerical complications with the conjugate gradient algorithm if two or more atoms would sit very close to each other and thus cause very large energies in the potential energy landscape. Comparisons of structures generated with the constraint of either 0.5 Å or 1.4 Å minimum allowed distance between the nearest neighboring atoms resulted in negligible differences. The computational cost was however improved significantly when using 1.4 Å as compared to 0.5 Å. Though by applying this constraint we introduce order, and we have to be cautious about starting the relaxation of the atoms from an already ordered state. A good measure of order is the characteristics of the RDF. The RDF of a perfect crystalline material will show the discrete peak positions of the 1st, 2nd, 3rd... and so forth nearest neighbor distances. If we take the perfect crystal and slightly distort the atomic positions, thus creating disorder, we will cause broadening of the peaks in the RDF. If we keep distorting then we will eventually have no structure at all, i.e. the pair distribution function is, for a large enough system, completely flat.

5.3 Voronoi Tessellation

Voronoi tessellation is a method that can be used for characterizing the short-range order of both amorphous and crystalline materials. Starting from any atom, lines are drawn to all nearby atoms. A perpendicular plane is drawn either at the midpoint between the atoms or at a point determined by the radii of atoms in the case of different species, e.g. the plane is drawn at the point where the atoms touch. In our calculations, we used half of the first peak position of the partial RDFs as the radii of the constituent atoms. The smallest enclosed volume is called a Voronoi polyhedron. Some of the surfaces of the polyhedra can be very small, with small in this case meaning that they only constitute a very small portion of the total surface area. We therefore introduce a cutoff for the smallest allowed/included surface area with respect to the total surface area. Figure 5.1 shows the average coordination number calculated from the Voronoi indexes as a function of relative surface area cutoff for $Fe_{0.93}Zr_{0.07}$, $Fe_{0.90}Zr_{0.10}$ and $Fe_{0.80}Zr_{0.20}$. We opted to use a 1% cutoff as it is near the inflection point of the first derivative. Each atom will have an associated polyhedron and the whole volume of the cell will be filled by these polyhedra without any gaps. Voronoi polyhedra are often used whenever the volume of an atom in a bulk material is needed, e.g. for integration of

the electron density to get the charge of an atom (cf. Bader charge analysis, Section 4.3).

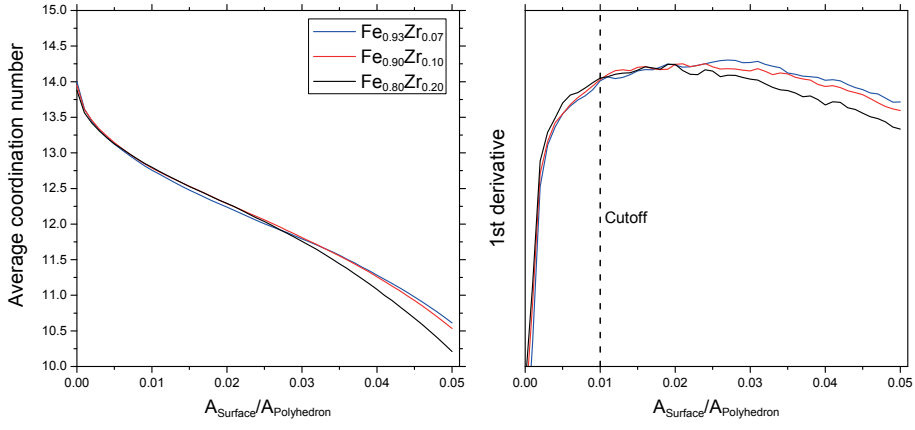

Figure 5.1. On the left hand side is the average coordination numbers as a function of relative area cutoff and on the right hand side is its first derivative. Dashed vertical line indicates the chosen cutoff.

The various polyhedra will be represented by Voronoi indexes in the form $\langle n_3, n_4, n_5, ... \rangle$ where n_i denotes the number of surfaces with i number of edges. For example, $\langle 0,6,0,0,0 \rangle$ denotes a shape with 6 faces, where, each face has 4 edges, i.e. a cube in the case of all faces being a square. The fraction of various polyhedra will give us in-depth information on the short-range structure. The set of polyhedra will, with great certainty, be unique for all amorphous materials and thus be a way to classify their individual structures. There will though, most likely, be a very large variety of polyhedra and most of them with very small fractions. When presenting data from Voronoi tessellation, it is common to only show the polyhedra that constitute more that a chosen minimum fraction of the total number of different polyhedra, as there will be, depending on the size of your system, a very large number of polyhedra.

From the Voronoi indexes we define the coordination number as $\sum_i n_i$, or in other words, the number of faces that constitute the polyhedron is the coordination number. The earlier mentioned polyhedra, $\langle 0,6,0,0,0 \rangle$, would then indicate a coordination number of 0+6+0+0+0=6.

We have used the software Voro++ to calculate the Voronoi indexes [79].

5.4 Results and discussion

We have investigated $Fe_{0.93}Zr_{0.07}$, $Fe_{0.90}Zr_{0.10}$ and $Fe_{0.80}Zr_{0.20}$ from both experiments and density functional calculations. Our aim is to evaluate the stochastic quenching method for amorphous $Fe_{1-x}Zr_x$ and how the structures

evolve when we alter the composition parameter x. From earlier experimental work, the amorphous FeZr displays varying critical magnetic temperature when the composition is changed [69]. Despite our calculations being non spin-polarized, we expect our structural characterization of these various compositions of Fe_xZr_{1-x} will provide some insight into the magnetic properties as the Fe-Fe distances and the coordination numbers are strongly correlated with the exchange energy.

Figure 5.2 shows the partial RDFs for $Fe_{0.93}Zr_{0.07}$, $Fe_{0.90}Zr_{0.10}$ and $Fe_{0.80}Zr_{0.20}$ where the sum of the partial constituents equal the total. The Zr-Zr data has also been given in separate boxes for better visibility. A common feature of all amorphous materials, per definition, is the lack of long-range order, i.e. g(r)=1 when r is large, where, $g(r)$ is the probability of finding another atom at a distance r from any reference atom. We can see in the RDF that there is almost no structural order beyond 7 Å and that $Fe_{0.80}Zr_{0.20}$ seems slightly more disordered than $Fe_{0.93}Zr_{0.07}$ and $Fe_{0.90}Zr_{0.10}$ as the RDF is flatter. Another distinct feature of an amorphous material is the so-called "splitting" of the second peak, which, for comparison, is not seen in liquids. The second and third peak, as indicated in the top RDF in Figure 5.2 with vertical lines, are properties of the RCP structure [3]. In the top left corner of Figure 5.2 is a simple illustration of the three distances that are indicated by vertical lines in the RDF.

Another attribute of the RDFs that stands it out is the shoulder on the first peak and it is clear that it is ascribed to the Fe-Zr partial RDF. In more general terms, we can say that the shoulder on the first peak is ascribed to the random packing of different size spheres.

To better quantify the RDF results, we provide Table 5.1 in which we list the distances to the first three peaks, where, the second and third peaks are given in units of the first peak position. A general trend that we can see is the decreasing of the Fe-Fe distance when the Zr content is increased. From earlier experimental work, an increase in average magnetic moment per Fe atom and Curie temperature was observed when the Zr content was increased up to a critical value [69]. This is consistent with lowering of the exchange energy when the Fe-Fe distance is shortened.

To provide more information on the short-range structure, we have performed Voronoi tesselation calculations from which we present the distribution of coordination numbers in Figure 5.3 and the fraction of different polyhedra in Figure 5.4. We can see that the distribution of coordination numbers becomes more smeared when we increase the Zr content. This is consequence of the different radii of the Fe and Zr atoms. A big atom can be encircled by many small atoms, which is the explanation for the bimodal appearance of the distribution [71]. The inverse case of a small atom being encircled by larger atoms is the explanation to the increase in smaller coordination numbers.

We limit the presented Voronoi polyhedra to those with a fraction of more than 0.01. The different shaded regions indicate a different number of sur-

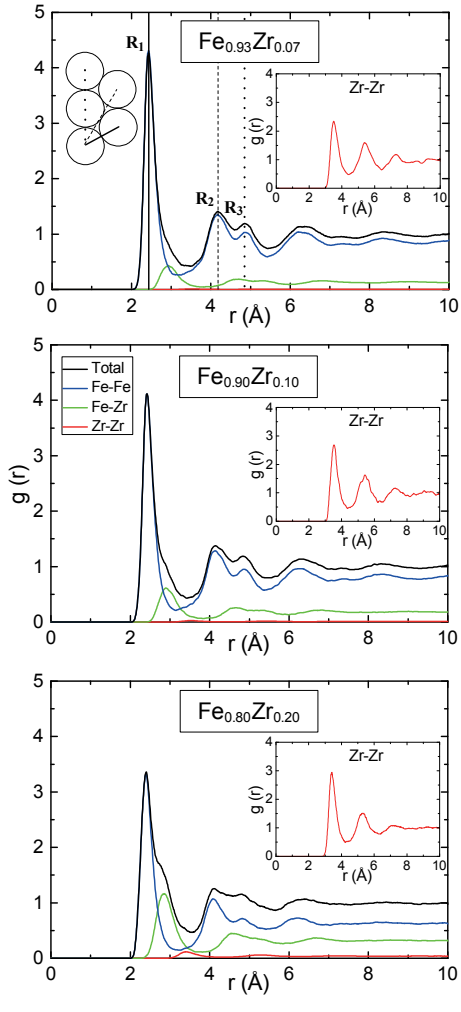

Figure 5.2. Radial distribution functions of $Fe_{0.93}Zr_{0.07}$, $Fe_{0.90}Zr_{0.10}$ and $Fe_{0.80}Zr_{0.20}$.

$\mathbf{Fe_{0.93}Zr_{0.07}}$	$\mathbf{R_1}$(Å)	$\mathbf{R_2/R_1}$	$\mathbf{R_3/R_1}$
Total	2.43	1.72	1.99
Fe-Fe	2.43	1.72	2.00
Fe-Zr	2.93	1.61	1.82
Zr-Zr	3.50	1.52	1.60
$\mathbf{Fe_{0.90}Zr_{0.10}}$	$\mathbf{R_1}$(Å)	$\mathbf{R_2/R_1}$	$\mathbf{R_3/R_1}$
Total	2.42	1.71	2.00
Fe-Fe	2.42	1.71	2.01
Fe-Zr	2.89	1.61	1.85
Zr-Zr	3.53	1.53	1.62
$\mathbf{Fe_{0.80}Zr_{0.20}}$	$\mathbf{R_1}$(Å)	$\mathbf{R_2/R_1}$	$\mathbf{R_3/R_1}$
Total	2.40	1.71	2.00
Fe-Fe	2.40	1.70	2.01
Fe-Zr	2.85	1.61	1.81
Zr-Zr	3.41	1.56	1.64

Table 5.1. *Peak positions in the radial distribution functions.*

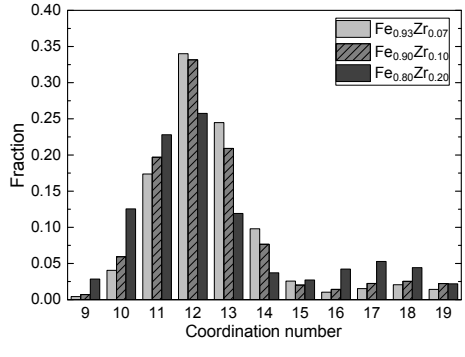

Figure 5.3. Fraction of different coordination numbers calculated from the mean number of surfaces of all Voronoi polyhedra.

faces (or coordination numbers) of the polyhedra. We can see a large degree of consistency in the close range structure, as several Voronoi polyhedra are reproduced in the three cases.

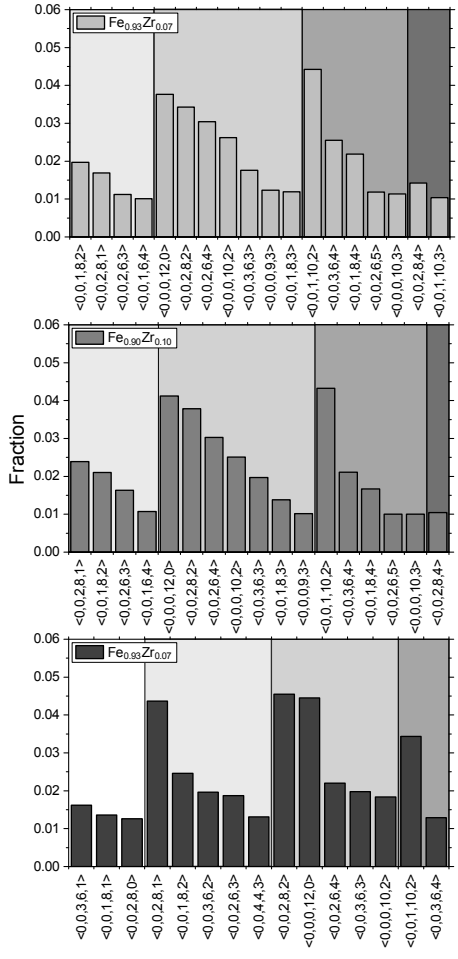

Figure 5.4. Fractions of Voronoi polyhedra where polyhedra with a fraction less than 0.01 have been excluded.

The physical significance of the near range order as described by Voronoi polyhedra requires further studies but it is very feasible that, for instance, the magnetic and mechanical properties can be interpreted from the Voronoi polyhedra.

6. Conclusions and outlook

We have demonstrated that first-principles Density Functional Theory (DFT) calculations can accurately describe the properties of hydrogen in metal. Our results are in good agreement with experimental findings for the investigated systems of V-H, $ScZr(CoNi)_2$-H, NdGa-H and GdGa-H. The focus of the work on hydrogen in vanadium has been the strain-induced effects on the potential energy landscape. We showed that the strain state of V-H has a profound effect on the phase diagram by comparing the stability of the different high symmetry interstitial sites for hydrogen occupancy as a function of c/a. We found that the preferred site occupancy is shifted from tetrahedral to octahedral when tensile strain is applied. The shift in site occupancy itself induces a change in the strain state of the system, from which we predict a hysteresis behavior in the volume/strain during the absorption and desorption of hydrogen in a clamped thin film of vanadium. The experimentally observed difference in the pressure-concentration isotherms for absorption and desorption in clamped vanadium films can be attributed to the proposed hysteresis from DFT calculations. The calculation for the $ScZr(CoNi)_2$-H system also deals with the stability of different interstitial sites, and the induced strain from hydrogen absorption. We compared experimental and theoretical results on the hydrogen-induced volume expansion and found good agreement. We also confirmed the expected near-linear volume increase with hydrogen concentration in transition metals.

From both Molecular Dynamics (MD) simulations and experimental measurements on the V-H system, we have found that the diffusion coefficient decreases significantly when strain is applied as the hydrogen atoms become more confined. The difference between tetrahedral and octahedral site occupancy is further investigated by comparing the heat of formation of hydrogen and deuterium to showcase the significance of zero point energy (ZPE) in the isotope effects. Fundamental research on the isotope effects can help promote applications for separation of the isotopes hydrogen, deuterium and tritium.

Vanadium-hydrogen is a good model system for investigations of metal-hydrogen interaction as it has a rather complex phase diagram which entails that there is a rich array of fundamental physics insights to be gathered from this system. From theory, we can calculate the free energy to be able to more accurately describe the phase transitions and to incorporate temperature and pressure in the static calculations. As we have so far focused on the effect of tensile strain on the potential energy surface, it would also be prudent to investigate the effect of compressive strain. It is reasonable to assume that compressive strain will promote quicker diffusion. From test calculations of

hydrogen in vanadium at the strain state of c/a=0.95 performed by us, we see a higher diffusion coefficient as compared to c/a$\geq$1.00. In material-based applications for hydrogen storage, the kinetics of diffusion is very important as the working temperature, for practical reasons, should be manageable from an engineering perspective. Thus, it is important to improve our understanding of the fundamental physics that governs the diffusion of lattice gases.

In the Zintl phase NdGa-H and GdGa-H systems, we investigated the bonding of the hydrogen atoms to rare earth and gallium atom. As these systems exhibit pronounced changes in structural and physical properties with the introduction of hydrogen, they can be considered good model systems for studies of hydrogen bonding. The structural properties determined from experiments are in good agreement with those calculated by DFT. We studied the partial density of states (DOS) and the Bader charges to determine how hydrogen was bonded to the material. These type of materials where hydrogen is covalently bound to p-block or rare earth metals are usually referred to as "chemical hydrides". Chemical hydrides are showing good promise concerning both gravimetric energy density and working temperature. A better understanding of the fundamental properties here could help to promote the needed research to meet the goals of stored energy per dollar/mass/volume to make hydrogen an economical and practical option as an energy carrier.

For the amorphous iron-zirconium, we investigated the level of accuracy at which we can describe this material using the stochastic quenching method. Comparison of structures generated with the stochastic quenching method with real samples that were structurally described by Extended X-ray Absorption Fine Structure (EXAFS). With structural agreement confirmed, we moved on to classify the structures by Radial Distribution Function (RDF) and polyhedra derived from Voronoi tessellation. Finding the correlation between the structure and the magnetic properties could, with the use of simple sphere-stacking models, allow us to create structures with desired magnetic properties. We found a shortening of the Fe-Fe bond when the Zr content was increased, which can explain the experimentally observed decrease in the magnetic moment and Curie temperature.

7. Svensk sammanfattning

Syftet med materialteori är att karaktärisera materials egenskaper utifrån interaktionerna mellan deras små beståndsdelar, atomkärnorna och elektronerna. Elektrisk ledningsförmåga, värmekapacitet, magnetiska och mekaniska egenskaper härrör alla från hur atomerna är ordnade i materialet och hur elektronerna är fördelade mellan atomerna för att, likt ett lim, hålla samman materialet genom den elektromagnetiska växelverkan. Vi kan exakt formalisera den elektromagnetiska växelverkan via Schrödingerekvationen. Det föreligger dock väldigt stora svårigheter att hitta en lösning på Schrödingerekvationen då vi vill beskriva ett system som innehåller fler än två partiklar. Vi kallar detta för ett flerkroppsproblem. Istället för att söka ett exakt sett att beskriva interaktionerna mellan dessa kroppar/partiklar så söker vi istället de bästa sätten att approximera dessa. I denna avhandling har vi tillämpat en första-princip metod baserad på täthetsfunktionalteori (Eng: density functional theory) som låter oss beräkna en god approximation till Schrödingerekvationen genom att behandla elektronerna som ett moln liggandes kring atomkärnorna. Molnet av elektroner kan beskrivas av en täthetsfunktional som endast beror av en parameter, vektorn $\mathbf{r}$. Framgången med täthetsfunktionalteori hänger mycket på hur väl vi kan beskriva elektron-elektron interaktionen. Täthetsfunktionalteorin formulerades redan 1965, på den tiden hade vi dock inte tillräckligt med datorkraft för att kunna behandla några större system med god noggrannhet. Täthetsfunktionaleorin sammanföll dock med en revolution inom integrerade kretsar som ledde till att datorer utvecklades i snabb takt. När datorerna blev bättre kunde större system behandlas och bättre approximationer för att beskriva elektron-elektron interaktionen kunde tillämpas. Idag kan många fysikaliska egenskaper i system innehållandes flera tusen atomer beskrivas med god precision.

I denna avhandling beskriver vi hur väte interagerar med övergångsmetaller, metaller från p-blocket och sällsynta jordartsmetaller. Syftet är att få en ökad förståelse för de fundamentala koncept som leder till att väte binder till metallen och hur vätet i sin tur också påverkar metallen. Väte orsakar små töjningar som globalt sett manifesterar sig som en ändring i volym. Vätet påverkar också det tidigare nämnda "molnet" av elektroner i metallen. Ändringen kan kartläggas genom att man beräknar elektronernas energier i metallen före och efter väte har absorberats för att på så vis kunna se vätets påverkan på elektronisk nivå.

Vi har undersökt hur väte i övergångsmetallen vanadin påverkas om vi töjer den. Töjning leder till att atom-atom avstånden ändras vilket i sin tur leder till

att elektronmolnet omkonfigureras. Vi har då på ett tillsynes enkelt sätt ändrat förhållandet för väteatomer i metallen. Vi beskriver detta som en ändring av energilandskapet. Att kunna förändra energilandskapet i en metall är ett sätt för oss att undersöka de fundamentala egenskaperna av väte i metall som nästan uteslutande beror av just energilandskapet. Vanadin är en extra intressant metall i detta avseende då den uppvisar en stor påverkan då den töjs. Som tidigare nämnt så ändras volymen av en metall när den absorberar väte, det är alltså inte bara en yttre påverkan som kan töja metallen, utan det sker också inifrån genom de sammanlagda små töjningarna orsakade av väteatomerna.

En väteatom bär på en elektron, denna elektron kommer att binda till en metall via delvis kovalenta, joniska och metalliska bindningar. Vi har undersökt hur väte binder till de sällsynta jordartsmetallerna neodymium och gadolinium samt gallium från p-blocket i periodiska systemet. I legeringar bestående av en sällsynt jordartsmetall och ett grundämne från p-blocket har väte en stor påverkan på elektronfigurationen, de lämpar sig därför till fundamental forskning om vätes inverkan.

För att sätta forskningen om väte i metall i ett större perspektiv så är det främst ett nytt medel för att lagra energi med en högre energitäthet per vikt- och volymenhet än vad dagens vanligt förekommande batterier kan erbjuda. Vätgasmolekyler bär på mycket energi då de gärna vill bilda nya föreningar med andra typer av atomer och på så vis frigöra energi i form av värme. En sådan förening är till exempel vatten (H_2O). En mix av väte och syre är därför väldigt lättantändlig och rik på energi. En förbränningsmotor som drivs på väte kommer alltså att producera utsläpp i form av vatten. En av de större utmaningarna med att driva en bil på vätgas är att få med sig vätet i bilen på ett säkert sätt. Den enklaste lösningen är att ta med sig vätet i gasform i en tryckbehållare. Risken det medför är dock att behållaren kan gå sönder och som följd kan vätgasen snabbt blandas med syre. Om man istället binder väte i en metall så kan inte vätet fly lika fort i händelse av att systemet skadas. Efterfrågan på stationära system för energilagring kommer också att öka i takt med att vi producerar mer förnyelsebar energi från till exempel vindkraft och solceller. Idag går mycket energi förlorad på grund av överproduktion, det vore därför bra att kunna lagra den energin för användning när produktionen inte motsvarar energiförbrukningen. Då väte i metall erbjuder en potentiellt stor mängd energi per volym och viktenhet så är det ett alternativ som måste utvärderas grundligt.

I sista delen av avhandlingen har vi undersökt det amorfa tillståndet av en legering bestående av järn och zirkonium. Att ett material är amorft innebär att det, till skillnad från ett kristallint, inte har en struktur som enkelt kan klassificeras med ett gitter och ett fåtal ordnade atomer (enhetscell). En amorf struktur kan enklast beskrivas som någonting oordnat men det är inte riktigt sant. Det måste finnas ordning i ett amorft material då det råder krafter mellan atomerna som inte kommer att tillåta att det inbördes avståndet mellan atomer blir för litet. Vi har tillämpat metoden stokastisk nedkylning (Eng: stochas-

tic quenching) för att generera amorfa strukturer. Metoden innebär att man börjar från en initialt slumpmässig ordning av atomer och därefter, med hjälp av täthetsfunktionalteori implementerad i ett datorprogram, beräkna krafterna mellan atomerna för att på så vis kunna uppdaterar atomernas positioner tills de resulterande krafterna på atomerna är väldigt nära noll. Gör man detta i små steg så kommer strukturen att hamna i ett så kallat metastabilt amorft tillstånd. Dessa av oss skapade strukturer från teoretiska modeller har blivit jämförda med riktiga prover av amorft järn-zirkonium. När vi kunde fastslå att vi med stokastisk nedkylning kunde skapa realistiska amorfa strukturer så var nästa steg att strukturellt definiera dessa strukturer. När sammansättningen av järn och zirkonium ändras så ändras också de fysiska egenskaperna hos materialet, bland annat ändras de magnetiska egenskaperna. Dessa ändringar kan med stor sannolikhet tillskrivas ändringarna av strukturen som en följd av ändringen i sammansättningen. Att kunna klassificera strukturen av ett amorft material där de fysikaliska egenskaperna ännu inte har mätts experimentellt kan ge oss en antydan om vad experimenten kommer att ge. I amorft järn-zirkonium kommer de magnetiska egenskaperna bero mycket på avståndet mellan järnatomerna och hur många av grannatomerna som också är järnatomer.

8. Acknowledgments

First and foremost I would like to thank my mom and dad for always being very supportive and for providing me with a good atmosphere to grow up in and for encouraging me to find the answers to the questions about the world of physics I have had for as long as I can remember.

I would not be writing this thesis if I were not given the opportunity to join the Materials Theory group at Uppsala University. So I would very much like to thank my supervisors Ralph, Olle and Rajeev for accepting my application and for all the support during my 5 years of Postgraduate studies.

In several scientific collaborations, I have met many researchers that have helped me open my mind and to look at research from many angles. A professor that stands out in this regard is Björgvin. I am very grateful for all the important lessons on many aspects of research that he brought to my attention. Following in his footsteps is his disciple Gunnar of whom I expect great things. Gunnar's burning passion and knowledge of science will take him far. I am thankful for the lessons of physics he gave me.

Another very fruitful collaboration was that with the chemistry boys: Jonas, Martin and Ulrich. I have been lucky to work with such brilliant, hard working and great guys through and through.

I would like to thank Petra, Giuseppe and Sebastian for the collaboration on the amorphous iron-zirconium project. It has been a long and bumpy ride and there is still some way to go but the educational value of traveling the bumpy road instead of the highway is invaluable. Thank you very much for being patient with me.

I have been blessed with great guys to share an office with. The first edition was Jonathan and Kostas. I was happy to learn that they both shared my love for awesome cheesy movies and that we shared the same, not so politically correct, sense of humor. Jonathan and Kostas were eventually replaced by two other great guys, Marco and Ritwik. It has been a pleasure sharing an office with those two very friendly and funny guys.

I want to thank Andreas for being a great friend, teaching partner and training partner. I want to thank my old friend and colleague John as it has been nice to have a familiar face around the office and someone who is always up for a fika on the weekends. I want to thank Dmitry for being a great friend and for helping me a lot with my research.

I have had the privilege of getting to know so many great people during my time as a Ph.D. student. I will not attempt to list them all. Their collective friendliness made the workplace a great one.

References

[1] P. Hohenberg and W. Kohn. Inhomogeneous electron gas. *Phys. Rev.*, 136:B864–B871, Nov 1964.

[2] Y. Fukai. *The Metal–Hydrogen System*, volume 21. Springer, 2005.

[3] R. Zallen. *The Physics of Amorphous Solids*. A Wiley-Interscience publication. Wiley, 1998.

[4] Ulrich Häussermann. Coexistence of hydrogen and polyanions in multinary main group element hydrides. *Zeitschrift fur Kristallographie*, 223(10):628–635, 2008.

[5] Ulrich Häussermann, Verina F. Kranak, and Kati Puhakainen. *Hydrogenous Zintl Phases: Interstitial Versus Polyanionic Hydrides*, pages 143–161. Springer Berlin Heidelberg, Berlin, Heidelberg, 2011.

[6] E. Holmström, N. Bock, T. Peery, E. Chisolm, R. Lizárraga, G. De Lorenzi-Venneri, and D. Wallace. Structure discovery for metallic glasses using stochastic quenching. *Physical Review B*, 82(2):024203, 2010.

[7] Nicolas Bock, Erik Holmström, Travis B. Peery, Raquel Lizárraga, Eric D. Chisolm, Giulia De Lorenzi-Venneri, and Duane C. Wallace. Liquid-state properties from first-principles density functional theory calculations: Static properties. *Physical Review B*, 82(14):144101, 2010.

[8] Krisztina Kádas, Matilda Andersson, Erik Holmström, Heiko Wende, Olof Karis, Sigita Urbonaite, Sergei M. Butorin, Sergey Nikitenko, Kristina O. Kvashnina, Ulf Jansson, and Olle Eriksson. Structural properties of amorphous metal carbides: Theory and experiment. *Acta Materialia*, 60(12):4720 – 4728, 2012.

[9] Louis Schlapbach and Andreas Züttel. Hydrogen-storage materials for mobile applications. *Nature*, 414(6861):353–358, 2001.

[10] Andreas Züttel, Arndt Remhof, Andreas Borgschulte, and Oliver Friedrichs. Hydrogen: the future energy carrier. *Philosophical Transactions of the Royal Society of London A: Mathematical, Physical and Engineering Sciences*, 368(1923):3329–3342, 2010.

[11] Andreas Züttel. Hydrogen storage methods. *Naturwissenschaften*, 91(4):157–172, 2004.

[12] Aron J. Cohen, Paula Mori-Sánchez, and Weitao Yang. Insights into Current Limitations of Density Functional Theory. *Science*, 2009.

[13] P. Hohenberg and W. Kohn. Inhomogeneous electron gas. *Phys. Rev.*, 136:B864–B871, Nov 1964.

[14] W. Kohn and L. J. Sham. Self-consistent equations including exchange and correlation effects. *Phys. Rev.*, 140:A1133–A1138, Nov 1965.

[15] J. P. Perdew, K. Burke, and M. Ernzerhof. Generalized gradient approximation made simple. *Phys. Rev. Lett.*, 77:3865–3868, 1996.

[16] J. P. Perdew, K. Burke, and M. Ernzerhof. Erratum: Generalized gradient approximation made simple. *Phys. Rev. Lett.*, 78:1396, 1997.

[17] Charles Kittel. *Introduction to Solid State Physics*. John Wiley & Sons, Inc., New York, 6th edition, 1986.
[18] N.W. Ashcroft and N.D. Mermin. *Solid State Physics*. Saunders College, Philadelphia, 1976.
[19] P. E. Blöchl. Projector augmented-wave method. *Phys. Rev. B*, 50:17953–17979, 1994.
[20] D. R. Hamann, M. Schlüter, and C. Chiang. Norm-conserving pseudopotentials. *Phys. Rev. Lett.*, 43:1494–1497, Nov 1979.
[21] G. Alefeld and J. Völkl. *Hydrogen in Metals I*, volume 28. Springer, 1978.
[22] G. Alefeld and J. Völkl. *Hydrogen in Metals II*, volume 29. Springer, 1978.
[23] Till Burkert, Andrius Miniotas, and Björgvin Hjörvarsson. Hydrogen-induced changes of the local structure in fe/v (001) superlattices. *Physical Review B*, 63(12):125424–, 2001.
[24] Robert Johansson, Rajeev Ahuja, Olle Eriksson, Björgvin Hjörvarsson, and Ralph H Scheicher. Effect of uniaxial strain on the site occupancy of hydrogen in vanadium from density-functional calculations. *Scientific reports*, 5(10301), 2015.
[25] H. Buck and G. Alefeld. Hydrogen in palladium–silver in the neighbourhood of the critical point. *Phys. Stat. Sol*, 49(1):317–327, 1972.
[26] G. Alefeld. *Ber. Bunsenges. Phys. Chem*, 76:746, 1972.
[27] U. Laudahn, S. Fähler, H. U. Krebs, and A. Pundt. Determination of elastic constants in thin films using hydrogen loading. *Appl. Phys. Lett.*, 74:647, 1999.
[28] M. Dornheim, A. Pundt, R. Kirchheim, S. J. v. d. Molen, E. S. Kooij, J. Kerssemakers, R. Griessen, H. Harms, and U. Geyer. Stress development in thin yttrium films on hard substrates during hydrogen loading. *Journal of Applied Physics*, 93(11):8958–8965, 2003.
[29] U. Laudahn, A. Pundt, M. Bicker, U. von Hülsen, U. Geyer, T. Wagner, and R. Kirchheim. Hydrogen-induced stress in nb single layers. *Journal of Alloys and Compounds*, 293—295(0):490 – 494, 1999.
[30] Andreas Blomqvist, Gunnar K. Pálsson, C. Moysés Araújo, Rajeev Ahuja, and Björgvin Hjörvarsson. Significance of self-trapping on hydrogen diffusion. *Phys. Rev. Lett.*, 105:185901, Oct 2010.
[31] Gunnar K. Pálsson, Moritz Wälde, Martin Amft, Yuanyuan Wu, Martina Ahlberg, Max Wolff, Astrid Pundt, and Björgvin Hjörvarsson. Hydrogen site occupancy and strength of forces in nanosized metal hydrides. *Phys. Rev. B*, 85:195407, May 2012.
[32] Stefan Olsson and Björgvin Hjörvarsson. Effect of biaxial elastic constraints on H − H interactions in ultrathin vanadium. *Phys. Rev. B*, 71:035414, Jan 2005.
[33] Xiao Xin, Gunnar K. Pálsson, Max Wolff, and Björgvin Hjörvarsson. Finite-size effects: Hydrogen in Fe/V(001) superlattices. *Phys. Rev. Lett.*, 113:046103, Jul 2014.
[34] G. Kresse and J. Hafner. Ab initio molecular dynamics for liquid metals. *Phys. Rev. B*, 47:558–561, 1993.
[35] G. Kresse and J. Hafner. Ab initio molecular-dynamics simulation of the liquid-metal-amorphous-semiconductor transition in germanium. *Phys. Rev. B*, 49:14251–14269, 1994.

[36] G. Kresse and J. Furthmüller. Efficiency of ab-initio total energy calculations for metals and semiconductors using a plane-wave basis set. *Comput. Mat. Sci.*, 6:15–50, 1996.
[37] G. Kresse and J. Furthmüller. Efficient iterative schemes for ab initio total-energy calculations using a plane-wave basis set. *Phys. Rev. B*, 54:11169–11186, 1996.
[38] D. Joubert G. Kresse. From ultrasoft pseudopotentials to the projector augmented-wave method. *Phys. Rev. B*, 59:1758–1775, 1999.
[39] Adolf A. Abrahamson. Born-mayer-type interatomic potential for neutral ground-state atoms with $z = 2$ to $z = 105$. *Phys. Rev.*, 178:76–79, Feb 1969.
[40] B Hjörvarsson, G Andersson, and E Karlsson. Metallic superlattices: Quasi two-dimensional playground for hydrogen. *J. Alloys Compd.*, 253:51–57, 1997.
[41] Garbriella Andersson, Per H. Andersson, and B. Hjörvarsson. Effects of varying compressive biaxial strain on the hydrogen uptake of thin vanadium (001) layers. *Journal of Physics*, 11(35):6669–6677, 1999.
[42] Per G. Sundell and Göran Wahnström. Self-trapping and diffusion of hydrogen in Nb and Ta from first principles. *Physical Review B - Condensed Matter and Materials Physics*, 70(22):1–7, 2004.
[43] Arnulf J. Maeland. Investigation of the vanadium—hydrogen system by x-ray diffraction techniques1,2. *The Journal of Physical Chemistry*, 68(8):2197–2200, 1964.
[44] Y. Ebisuzaki and M. O'Keeffe. The solubility of hydrogen in transition metals and alloys. *Progress in Solid State Chemistry*, 4:187 – 211, 1967.
[45] P.C.P. Bouten and A.R. Miedema. On the heats of formation of the binary hydrides of transition metals. *Journal of the Less Common Metals*, 71(1):147 – 160, 1980.
[46] P Nordlander, J K Norskov, and F Besenbacher. Trends in hydrogen heats of solution and vacancy trapping energies in transition metals. *Journal of Physics F: Metal Physics*, 16(9):1161, 1986.
[47] Yuh Fukai. State of hydrogen in bcc metals: Its quantum-mechanical character. *Japanese Journal of Applied Physics*, 22(2R):207, 1983.
[48] Per H. Andersson, Lars Fast, Lars Nordström, Börje Johansson, and Olle Eriksson. Theoretical study of structural and electronic properties of vh_x. *Phys. Rev. B*, 58:5230–5235, Sep 1998.
[49] C. D. Gelatt, A. R. Williams, and V. L. Moruzzi. Theory of bonding of transition metals to nontransition metals. *Physical Review B*, 27(4):2005–2013, 1983.
[50] H Peisl. *Lattice strains due to hydrogen in metals*, volume 28 of *Topics in Applied Physics*. Springer Berlin, 1978.
[51] Adolph Fick. On liquid diffusion. *Journal of Membrane Science*, 100(1):33–38, 1995.
[52] Robert Brown. A brief account of microscopical observations made in the months of June, July and August, 1827, on the particles contained in the pollen of plants; and on the general existence of active molecules in organic and inorganic bodies. 1828.
[53] A. Einstein. Zur Theorie der *Brownschen* Bewegung. (German) [On the theory of Brownian motion]. 324(2):371–381, 1906.

[54] Helmut Wipf. *Hydrogen in Metals III*, volume 73 of *Topics in Applied Physics*. Springer Berlin Heidelberg, 1997.
[55] Yinggang Li and Göran Wahnström. Molecular-dynamics simulation of hydrogen diffusion in niobium. *Phys. Rev. B*, 51:12233–12245, May 1995.
[56] C T Chudley and R J Elliott. Neutron scattering from a liquid on a jump diffusion model. *Proceedings of the Physical Society*, 1(2):353, 1961.
[57] C. P. Flynn and A. M. Stoneham. Quantum theory of diffusion with application to light interstitials in metals. *Phys. Rev. B*, 1:3966–3978, May 1970.
[58] K Itoh and T Fukunaga. Short-range structure of β-VD: Pair distribution function analysis of x-ray and neutron diffraction. *Journal of Applied Physics*, 2007.
[59] J.M. Rowe, Kurt Sköld, H.E. Flotow, and J.J. Rush. Quasielastic neutron scattering by hydrogen in the α and β phases of vanadium hydride. *Journal of Physics and Chemistry of Solids*, 32(1):41–54, 1971.
[60] Kohta Asano, Shigenobu Hayashi, Yumiko Nakamura, and Etsuo Akiba. Effect of substitutional mo on diffusion and site occupation of hydrogen in the {BCT} monohydride phase of v–h system studied by 1h {NMR}. *Journal of Alloys and Compounds*, 507(2):399 – 404, 2010.
[61] Zh Qi, J Volkl, R Lasser, and H Wenzl. Tritium diffusion in V , Nb and Ta. *J. Phys. F: Met. Phy*, 13:2053–2062, 1983.
[62] ‡ Thomas Björling, ‡ Dag Noréus, , and § Ulrich Häussermann*, †. Polyanionic hydrides from polar intermetallics aee2 (ae = ca, sr, ba; e = al, ga, in). *Journal of the American Chemical Society*, 128(3):817–824, 2006. PMID: 16417371.
[63] H. J. Monkhorst and J. D. Pack. *Phys. Rev. B*, 13:5188, 1976.
[64] W Tang, E Sanville, and G Henkelman. A grid-based bader analysis algorithm without lattice bias. *Journal of Physics: Condensed Matter*, 21(8):084204, 2009.
[65] Edward Sanville, Steven D. Kenny, Roger Smith, and Graeme Henkelman. Improved grid-based algorithm for bader charge allocation. *Journal of Computational Chemistry*, 28(5):899–908, 2007.
[66] Eugen Axinte. Metallic glasses from " alchemy" to pure science: Present and future of design, processing and applications of glassy metals. *Materials and Design*, 35:518–556, 2012.
[67] W L Johnson. Bulk amorphous metal—An emerging engineering material. *Jom*, 54(3):40–43, 2002.
[68] Chaoming Song, Ping Wang, and Hernán A. Makse. A phase diagram for jammed matter. *Nature*, 453(7195):629–632, 2008.
[69] Atieh Zamani, Anders Hallén, Per Nordblad, Gabriella Andersson, Björgvin Hjörvarsson, and Petra E. Jönsson. Tuning magnetic properties by hydrogen implantation in amorphous thin films. *Journal of Magnetism and Magnetic Materials*, 346:138 – 141, 2013.
[70] Robert S. Farr and Robert D. Groot. Close packing density of polydisperse hard spheres. *Journal of Chemical Physics*, 131(24), 2009.
[71] Kristin Lochmann, Luc Oger, and Dietrich Stoyan. Statistical analysis of random sphere packings with variable radius distribution. *Solid State Sciences*, 8(12):1397–1413, 2006.

[72] G D Scott and D M Kilgour. The density of random close packing of spheres. *Journal of Physics D: Applied Physics*, 2(6):863, 1969.
[73] D B Miracle. A structural model for metallic glasses. *Nat Mater*, 3(10):697–702, 2004.
[74] Zbigniew H Stachurski. Definition and properties of ideal amorphous solids. *Physical review letters*, 90(15):155502, 2003.
[75] L. Vegard. Die konstitution der mischkristalle und die raumfüllung der atome. *Zeitschrift für Physik*, 5(1):17–26, 1921.
[76] R. N. Barnett, C. L. Cleveland, and Uzi Landman. Structure and dynamics of a metallic glass: Molecular-dynamics simulations. *Phys. Rev. Lett.*, 55:2035–2038, Nov 1985.
[77] J.M. Thijssen. *Computational Physics*. Cambridge University Press, 1999.
[78] R.M. Martin. *Electronic Structure: Basic Theory and Practical Methods*. Cambridge University Press, 2004.
[79] Chris H. Rycroft. Voro++: A three-dimensional voronoi cell library in c++. *Chaos*, 19(4), 2009.

Acta Universitatis Upsaliensis

Digital Comprehensive Summaries of Uppsala Dissertations from the Faculty of Science and Technology 1396

Editor: The Dean of the Faculty of Science and Technology

A doctoral dissertation from the Faculty of Science and Technology, Uppsala University, is usually a summary of a number of papers. A few copies of the complete dissertation are kept at major Swedish research libraries, while the summary alone is distributed internationally through the series Digital Comprehensive Summaries of Uppsala Dissertations from the Faculty of Science and Technology. (Prior to January, 2005, the series was published under the title "Comprehensive Summaries of Uppsala Dissertations from the Faculty of Science and Technology".)

Distribution: publications.uu.se
urn:nbn:se:uu:diva-299940

ACTA
UNIVERSITATIS
UPSALIENSIS
UPPSALA
2016